xDDx: a Numerical Toolbox for Ultrasound Transducer Characterization and Design with Acoustic Holography

Pavel B. Rosnitskiy, Oleg A. Sapozhnikov, Vera A. Khokhlova, Wayne Kreider, Sergey A. Tsysar, Gilles P.L. Thomas, Kaizer Contreras, and Tatiana D. Khokhlova

***Abstract*— Transient acoustic holography is a useful technique for characterization of ultrasound transducers. It involves hydrophone measurements of the 2-D distribution of acoustic pressure waveforms in a transverse plane in front of the transducer – a hologram – and subsequent numerical forward or backward projection of the ultrasound field. This approach enables full spatiotemporal reconstruction of the acoustic field, including the vibrational velocity at the transducer surface. This allows identification of transducer defects as well as structural details of the radiated acoustic field such as side lobes and hot spots. However, numerical projections may be time-consuming (10^{10} – 10^{11} operations with complex exponents). Moreover, back-projection from the measurement plane to the transducer surface is sensitive to misalignment between the axes of the positioning system and the axes associated with the transducer. This paper presents an open access transducer characterization toolbox for use in MATLAB or Octave on Windows computers (https://github.com/pavrosni/xDDx/releases). The core algorithm is based on the Rayleigh integral implemented in C++ executables for graphics and central processing units (GPUs and CPUs). The toolbox includes an automated procedure for correcting axes misalignments to optimize the visualization of transducer surface vibrations. Beyond using measured holograms, the toolbox can also simulate the fields radiated by user-defined transducers. Measurements from two focused 1.25-MHz 12-element sector transducers (apertures of 87 mm, focal distances of 65 mm and 87 mm) were used with the toolbox for demonstration purposes. Simulation speed tests for different computational devices showed a range of 0.2 s – 3 min for GPUs and 1.6 s – 57 min for CPUs.**

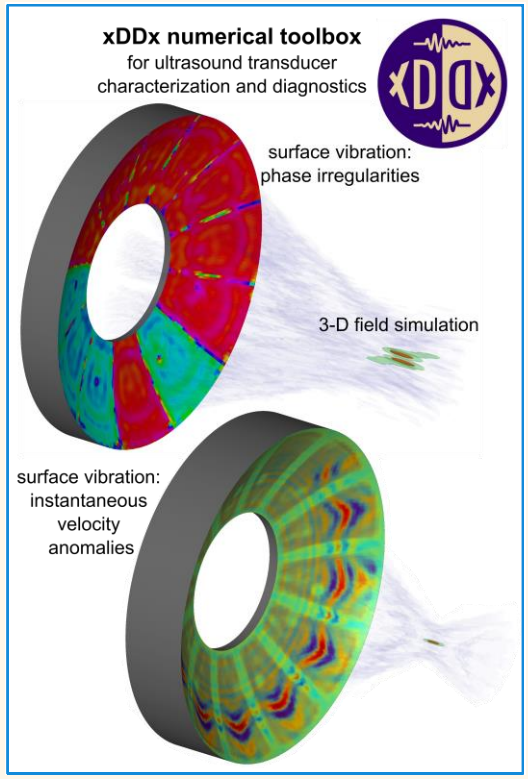

***Index Terms*— Acoustic holography, high-intensity focused ultrasound (HIFU), CUDA, GPU, simulation, toolbox, open access**

I. Introduction

The ability to comprehensively and consistently characterize the fields radiated by ultrasound transducers is a critical part of the development and implementation of medical ultrasound technologies. Over many years, standardized measurement techniques have been developed to characterize the three-dimensional (3-D) structure of the radiated beam as well as the corresponding acoustic power [1, 2]. Although power measurements can be conducted in different ways, hydrophone measurements are an essential part of field characterization [3]. As described in a recent review article [4], the measurement process typically includes selection of a suitable hydrophone and use of a scanning tank filled with water to perform computer-controlled recording of pressure waveforms in a way that coordinates transducer excitation, waveform digitization, and hydrophone motion in the ultrasound field of interest. Two-dimensional (2-D) planar scans with a hydrophone are of particular interest here because of the potential to obtain acoustic holography data from a simple scan [5 – 8]. Acoustic holography includes the measurement process and numerical processing steps in which (a) the planar scan data are processed into a hologram comprising pressure magnitude and phase information at each scan location, and (b) the hologram is numerically projected forward or backward to simulate linear acoustic propagation and reconstruct the full 3-D field. The use of such reconstructions to evaluate the field structure is described in an international technical specification for therapeutic ultrasound fields [9]. Such an approach is much more efficient in

This work was supported in part by NIH under Grants R01EB025187, R01AR080120, R01EB031788, and R01EB007643. (Corresponding author: Pavel B. Rosnitskiy.). Please see the Acknowledgment section of this article for the author affiliations.

Highlights

- **An open access numerical toolbox for post-processing measured acoustic holograms has been developed to characterize the vibrations of ultrasound sources and simulate 3-D acoustic fields.**
- **The toolbox includes the algorithms for fast Rayleigh Integral simulations on GPUs and CPUs, along with options for automatic correction of the position uncertainties of the transducer.**
- **Performance of the toolbox was demonstrated using transient holograms measured for two focused 12-element transducers with slight manufacturing defects.**

quantifying the 3-D field in comparison with performing 3-D hydrophone scans. Because therapeutic applications often involve array transducers with multiple focusing configurations and corresponding 3-D fields, the efficiency of holography techniques is particularly valuable [10].

In addition to characterizing the 3-D field radiated into water, acoustic holography can also be used to reconstruct the transducer vibrations to (a) visualize and quantify any irregularities and (b) define a boundary condition for modeling the field at elevated output levels and/or in media other than water [11 – 13]. Knowledge of the vibrational velocity pattern at the transducer surface can reveal manufacturing defects that manifest as amplitude and phase nonuniformity, potentially leading to poor focusing or device failure. Moreover, detailed characterization of the transducer vibrations of multi-element arrays can be used to understand and possibly improve array focusing while minimizing grating lobes [14 – 20].

Current implementations of acoustic holography begin with a planar hydrophone scan and the recording of pressure waveforms at (typically) tens of thousands of points in a uniformly spaced grid, as illustrated in Fig. 1(a, b). This collection of waveforms is then processed into a hologram – a 2-D record of the magnitude and phase of the acoustic pressure field. If the magnitude and phase are only recorded at a single frequency, then the hologram represents a continuous-wave (CW) field. If they are recorded over a range of frequencies, typically corresponding to a short transducer excitation that lasts for no more than a few acoustic cycles then the hologram represents a transient field. Therefore, transient holograms allow for broadband transducer characterization [21 – 23]. For both CW and transient regimes, the full 3-D field represented by the hologram can be numerically reconstructed by forward projection (FP) and backward projection (BP) calculations.

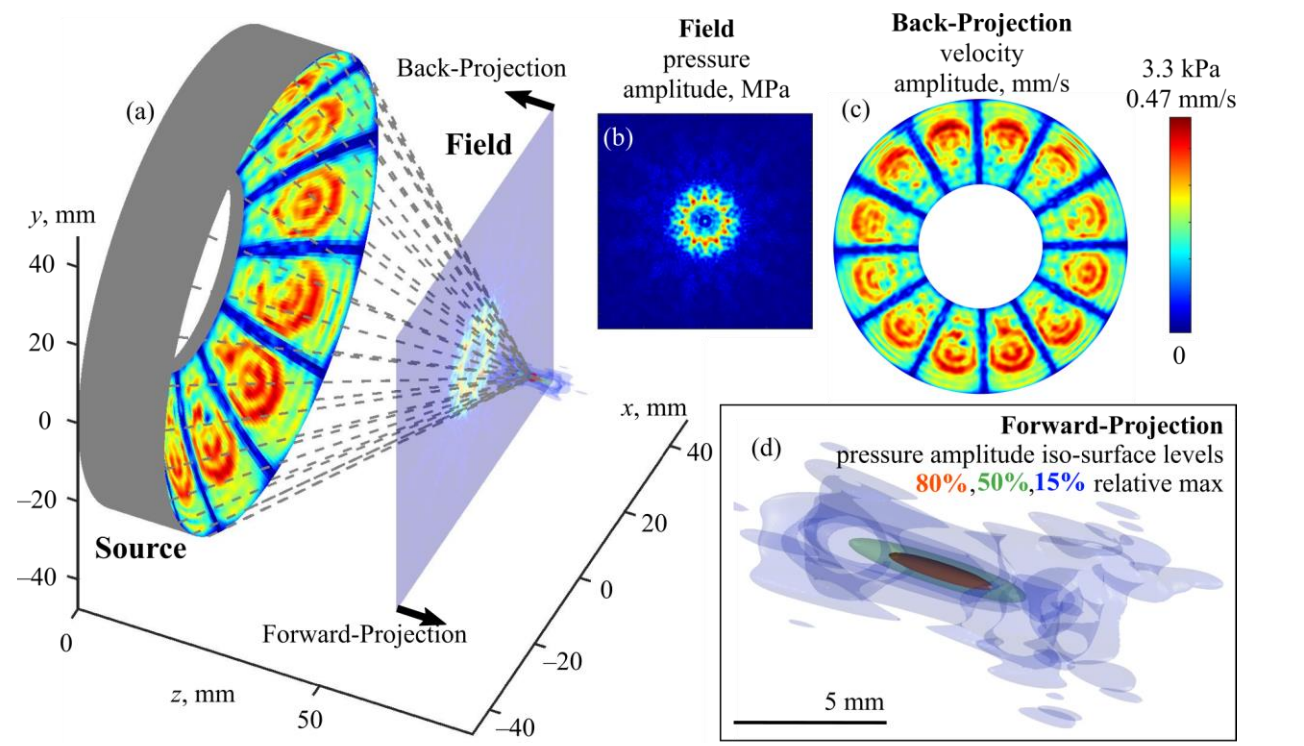

Fig. 1. Example of a typical implementation of acoustic holography for a 1.25-MHz transducer with nominal aperture 87 mm and focal distance 65 mm: (a) 3-D illustration of the geometry of the planar scan and forward- and back-projections (FP and BP); (b) pressure amplitude in the scan plane; (c) normal velocity distribution on the surface of the transducer obtained by BP; and (d) 3-D field in the focal region obtained by FP.

Useful reconstructions often include locations that represent the transducer surface (Fig. 1(c)) and regions of interest near the focus (Fig. 1(d)).

Performing the projection calculations relies on a model-based formulation of lossless, linear wave propagation in water. Common formulations of acoustic holography are based on either an angular spectrum solution or the Rayleigh integral, as discussed in more detail by Sapozhnikov *et al*. [8]. For medical ultrasound transducers that are often focused, the Rayleigh integral formulation is appealing because it is readily applicable to reconstructions on curved surfaces and it permits point-by-point corrections related to changing conditions during planar scan measurements (*i.e.*, changes in water temperature). Under these practical conditions, accurate field reconstructions have been shown to be feasible [8, 13, 15, 18 – 20, 22, 24– 27].

Although transient holography is broadly useful as the most general approach for characterizing transducers, a key challenge in its implementation is that a large number of computational operations with complex numbers are required. For example, consider a typical hologram with 150 spectral components across a spatial grid of 180×180 vertices. Numerical projection to another target grid with the same 180×180 number of vertices, but not necessarily the same spatial grid step, requires calculating a propagation distance R for each pair of points of the initial 180^2-point grid and the second 180^2-point grid. This results in 180^4 operations. Given that the Rayleigh integral requires the calculation of complex exponents of the type $\exp(\pm ikR)$ for each of the 150 frequency components with a wavenumber k, the total number of operations is $180^4 \cdot 150 = 1.6 \cdot 10^{11}$.

This makes postprocessing time-consuming and points to a practical need for fast methods of transient holography projection [21, 26]. Although computational complexity could be reduced by using an angular spectrum formulation rather than the Rayleigh integral, the geometric flexibility noted above for the Rayleigh integral remains compelling to facilitate reconstructions of transducer surface vibrations. Another advantage of the Rayleigh integral over the angular spectrum method is that it does not suffer from spatial aliasing errors, as it is not based on spectral transforms.

Another practical challenge for holographic transducer characterization pertains to alignment. For planar scan measurements, the transducer is often (and most conveniently) held in the water tank with manually oriented fixturing. Consequently, the transducer alignment relative to the axes of the positioning system and the scan plane is known only approximately. Potential misalignment between the transducer's acoustical coordinates and the positioner's mechanical coordinates is depicted in Fig. 2(a). Given a typical rotational error of 1° (0.018 radians) for a visually aligned transducer and a hologram axial distance from the source of 50 wavelengths (50λ), the linear displacement error after back-projection would be about $0.018 \cdot 50\lambda \approx \lambda$, thus resulting in noticeable phase errors at the surface of the reconstructed source [28]. Because such an angular misalignment is nontrivial, complete implementations of holography should include alignment correction when transducer surface vibrations are reconstructed for quantitative evaluations.

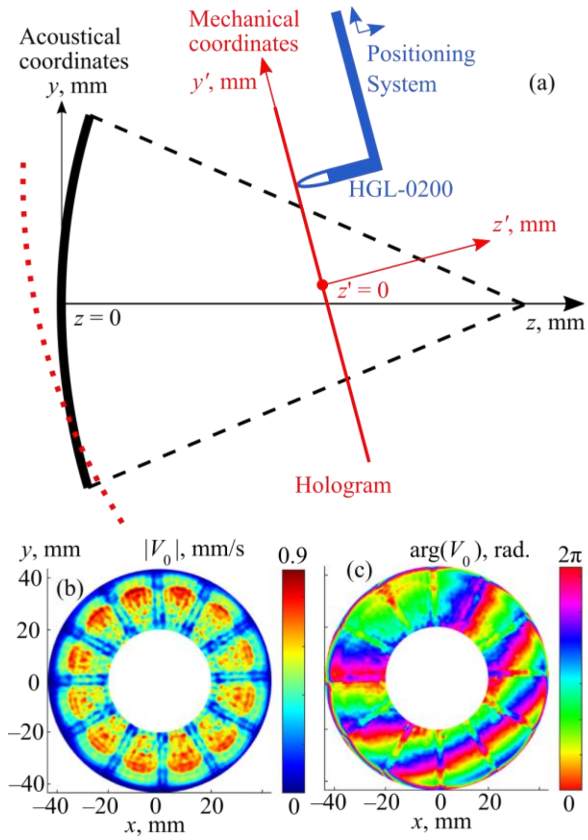

Fig. 2. The impact of angular misalignment between the positioning system and the transducer. The top schematic (a) illustrates the geometry of mechanical and acoustical coordinates. The bottom plots (b, c) show sample back-projection results for transducer surface velocity magnitude and phase without correction for misalignment. Results come from the transducer mentioned in Fig. 1 at the nominal frequency of f_0 = 1.25 MHz. Despite the presence of multiple phase cycles in the reconstruction, the excitation phase was uniform.

Alignment correction can be performed from the recorded hologram because it does indeed contain information about the entire 3-D field. Starting with a hologram from a planar scan in mechanical coordinates, the relative orientation of the acoustic axis of a focused source can typically be determined by projecting the field to multiple transverse planes near the focus, finding the location of the pressure maximum in each plane, and drawing a line through these maxima [18, 28]. Although such angular corrections for locating the transducer surface are possible, they can add nontrivial computational expense to implementations of transient holography.

The aim of this paper is to present an approach and corresponding numerical toolbox to facilitate the practical implementation of transient holography for characterizing ultrasound fields and the corresponding transducer vibrations. Key capabilities are fast post-processing of recorded planar hydrophone scan data to define transient holograms, rapid back-projection onto the transducer surface, and rapid 3-D field simulation. The toolbox also includes a new algorithm for automatic alignment corrections for strongly focused transducers. The open-access toolbox is designed to function as a part of MATLAB (MathWorks, Inc., Natick, MA, USA) or Octave (free software http://www.octave.org) computing environments on personal computers running a Windows operating system (Microsoft Inc., Redmond, WA, USA). This software is named the xDDx toolbox and is available from the link https://github.com/pavrosni/xDDx/releases. In the name, "xD" is a shorthand for "transducer" and "Dx" is a familiar shorthand reference for "diagnostics". The xDDx algorithms were developed in two versions: for compute unified device architecture (CUDA-compatible graphics processing units – GPUs), and for central processing units (CPUs). The algorithms were specifically optimized for speed and can be used both for post-processing of planar scan data into holograms and for field projection calculations. In addition to details about the toolbox itself, this paper also presents a demonstration of xDDx toolbox capabilities for two examples of strongly focused HIFU transducers.

II. Materials and Methods

A. Transient Hologram and its Fourier Decomposition

A transient hologram is a record of the transverse distribution of the temporal profile of acoustic pressure on a certain extended section of the surface through which the radiated wave beam passes (Fig. 1(a)). In practice, a hologram is usually recorded on a flat, rectangular (usually square) surface using planar scanning of the field by a hydrophone, which is moved by an automated positioning system. The acoustic source is repeatedly excited by identical short pulses, and the hydrophone moves and records the signal sequentially at each scan point with a step size between points of less than a half wavelength at the center frequency of the excitation.

The recorded pressure pulses at each point of the hologram can be represented as a 3-D matrix $p_{\mathrm{H}}(x_l{}', y_m{}', t_s)$. Here $(x_l{}', y_m{}')$ are the coordinates of the points on the hologram grid, defined in such a way that the origin of the coordinate system is located at the center of the hologram: $x_l{}' = [l - (L+1)/2] \cdot \Delta x_H$, $y_m{}' = [m - (M+1)/2] \cdot \Delta y_H$, where $l = 1, \dots, L$ and $m = 1, \dots, M$ (the numbers L and M are assumed to be odd), and $t_s = s \cdot \Delta t$ is the time sample of the signal recorded by the digitizer with a time step Δt, $s = 0, \dots, N$, where N is the number of time points in the recorded waveform. Typically, the numbers L and M are of the order of a hundred or several hundred, and N is of the order of several thousand.

The spectral decomposition of the pressure matrix $p_H(x_l{}', y_m{}', t_s)$ can be represented as a sum of harmonic waves at different frequencies f_n using the Inverse Discrete Fourier Transform (IDFT) [8, 29]:

$$p_s(x_l', y_m') = \frac{1}{N} \sum_{n=0}^{N-1} \hat{p}_n\,(x_l{}', y_m{}') e^{2\pi i f_n t_s}. \tag{1}$$

Here, $p_s(x_l', y_m') = p_{\mathrm{H}}(x_l{}', y_m{}', t_s)$ represents discretized version of the pressure temporal waveform, i is the imaginary unit, $\hat{p}_n$ is the complex amplitude of a spectral component of the signal at the frequency $f_n = n \cdot \Delta f$ ("single-frequency" component), and $\Delta f = (N \cdot \Delta t)^{-1}$ is the frequency step. Here we assume the $e^{+2\pi i f t}$ convention for the complex representation of waves travelling forward. The complex amplitudes $\hat{p}_n$ can be expressed utilizing the direct Discrete Fourier Transform (DFT):

$$\hat{p}_n(x_l{}', y_m{}') = \sum_{s=0}^{N-1} p_s(x_l', y_m')\, e^{-2\pi i f_n t_s}. \tag{2}$$

This paper uses a less common single-sided form of the IDFT (1) which is more intuitive for applications in acoustics:

$$p_{\mathrm{H}}(x_l{}', y_m{}', t_s) \approx \sum_{n=0}^{N_{\max}} |P_n| \cos(2\pi f_n t_s + \arg(P_n))\,, \tag{3}$$

where $P_n(x_l{}', y_m{}')$ is a single-sided complex amplitude at the frequency f_n, $|P_n|$ is its magnitude, $\arg(P_n)$ is its phase, and $N_{\max} < N/2$ is the frequency sample number for the highest significant spectral component. The conversion between the conventional (1) and the single-sided (3) forms is well known and is described in the xDDx documentation [30].

In the case of the hologram signals, we denote the single-sided spectrum P_n as H_n to emphasize that we are describing the hologram in the scan plane: $P_n = H_n$.

Thus, different single-frequency components $|H_n|\cos(2\pi f_n t_s + \arg(H_n))$ can be projected either forward or backward using the Rayleigh integral simulator implemented in the toolbox. For linear acoustic propagation, single-frequency components H_n can be projected independently; then the time-domain pressure signal at each reconstruction point is recovered through application of the IDFT in (3) [21].

B. Rayleigh Integral Simulation Algorithm

The algorithms presented here are based on numerical calculation of the Rayleigh integral. To be more general, in this subsection we consider a hologram defined in a coordinate system with the origin not necessarily lying in the plane of the experimentally recorded hologram. Let the hologram be defined in the coordinate system (x, y, z) and located in the plane $z = z_H$, with the pressure specified at the following grid points: $\mathbf{r}_{lm} = (x_l, y_m, z_H)$, $x_l = [l - (L+1)/2] \cdot \Delta x_H$, $y_m = [m - (M+1)/2] \cdot \Delta y_H$, where $\mathbf{r}_{lm}$ is the position vector for a given point in the hologram, $l = 1, \dots, L$ and $m = 1, \dots, M$. A detailed explanation of the corresponding equations for different projection cases is provided elsewhere [8]. Here we present only specific examples of forward and backward projection equations.

The first example shows the case of forward projection (away from the transducer) of the single-frequency complex pressure amplitude $H_n(x_l, y_m)$ as a summation over all points in the hologram to obtain the 3-D complex pressure amplitude distribution P_n:

$$P_n(\mathbf{r}) = \Delta S \sum_{l=1}^{L} \sum_{m=1}^{M} H_n(x_l, y_m)\, K_{\mathrm{pp}}^{\mathrm{fwd}}(x_l, y_m; \mathbf{r})\,. \tag{4}$$

Here $\mathbf{r} = (x, y, z)$ is the position vector for a given field reconstruction point, $\Delta S = \Delta x_H \Delta y_H$ is the elemental surface area corresponding to each discretized hologram point, and summations over subscripts l and m represent the numerical implementation of the surface integral. The forward-projection ("fwd") kernel with pressure input and pressure output ("pp") can be expressed as follows:

$$K_{\mathrm{pp}}^{\mathrm{fwd}}(x_l, y_m; \mathbf{r}) = \frac{(z - z_H) \cdot \left(\frac{ik_n}{R_{lm}} + \frac{1}{R_{lm}^2}\right)}{2\pi R_{lm}} \cdot e^{-ik_n R_{lm}} \qquad (5)$$

where $k_n = 2\pi f_n / c_0$ is the wavenumber, c_0 is the sound speed in water, $R_{lm} = |\mathbf{r}_{lm} - \mathbf{r}|$.

Note that to match the choice of sign of the exponent in MATLAB/Octave when computing the FFT, $K_{\mathrm{pp}}^{\mathrm{fwd}}$ in (5) is the complex conjugate of $K_{\mathrm{pp}}^{\mathrm{fwd}}$ presented in [8], since here in (1) we adopted the convention $e^{+2\pi ift}$ to represent the forward-propagating wave, whereas in [8] $e^{-2\pi ift}$ is assumed instead. The same change is made for $K_{\mathrm{pv}}^{\mathrm{bwd}}$ below.

The second example demonstrates the back-projection of the same scan-plane hologram $H_n(x_l, y_m)$ onto a spherical transducer surface with radius of curvature F. Considering the geometry in Fig. 1(a) with the transducer apex at the origin, the transducer surface is defined as the set of points that satisfy the equation $z = F - \sqrt{F^2 - x^2 - y^2}$. Then the complex amplitude of the normal velocity V_n on the transducer surface is obtained from

$$V_n(\mathbf{r}) = \Delta S \sum_{l=1}^{L} \sum_{m=1}^{M} H_n(x_l, y_m) K_{\mathrm{pv}}^{\mathrm{bwd}}(x_l, y_m; \mathbf{r}) \,. \qquad (6)$$

In this case $\mathbf{r}$ is a position vector that defines a point on the transducer surface, and the back-projection ("bwd") kernel with pressure input and velocity output ("pv") is [8]

$$K_{\mathrm{pv}}^{\mathrm{bwd}}(x_l, y_m; \mathbf{r}) = e^{ik_n R_{lm}} \times \frac{A\left(\frac{-ik_n}{R_{lm}} + \frac{1}{R_{lm}^2}\right) + B\left(\frac{-3ik_n}{R_{lm}} + \frac{3}{R_{lm}^2} - k_n^2\right)}{-2\pi i k_n \rho_0 c_0 R_{lm}} \qquad (7)$$

where $A = (\mathbf{n}_1 \cdot \mathbf{n}_2)$, $B = -(\mathbf{d}_{lm} \cdot \mathbf{n}_1)(\mathbf{d}_{lm} \cdot \mathbf{n}_2)$, $\mathbf{d}_{lm} = (\mathbf{r}_{lm} - \mathbf{r})/R_{lm}$, $\mathbf{n}_1 = -(x, y, z - F)/F$, $\mathbf{n}_2 = (0,0,-1)$, ρ_0 is the water density, and, as defined earlier, $k_n = 2\pi f_n / c_0$ is the wavenumber and c_0 is the sound speed in water.

For both forward- and back-projection cases described by (4) and (6), the resulting projection $Q_n(\mathbf{r})$ (Q being either P or V) is calculated as a sum of the element-wise product of the hologram matrix and the kernel matrix:

$$Q_n(\mathbf{r}) = \sum_{l=1}^{L} \sum_{m=1}^{M} H_n(x_l, y_m)\, K(x_l, y_m; \mathbf{r}), \qquad (8)$$

where $K = \Delta S \cdot K_{\mathrm{pv}}^{\mathrm{bwd}}$ or $K = \Delta S \cdot K_{\mathrm{pv}}^{\mathrm{bwd}}$. Even though kernel $K(x_l, y_m; \mathbf{r})$ matrices differ for different projection cases (forward/backward), different outputs (pressure/velocity), and different surface shapes (flat/spherical), the general structure of the calculation expression (8) remains the same.

In the xDDx numerical toolbox, computational algorithms for (8) are implemented in C++, with separate versions for execution on GPUs and CPUs. The first version for CUDA-compatible GPUs was designed to be efficient for large numbers of GPU threads that significantly exceed those available for CPUs. To take advantage of this, the output points $\mathbf{r}$ and frequency samples n were redistributed among GPU threads and the corresponding (l, m) sums were independently calculated.

The same computational algorithm could be applied to the CPU version, which, however, would have significantly lower computational speed due to the availability of fewer cores. To improve performance for CPU users, the sum of the element-wise product by indexes (l, m) was performed using an open-source C++ library "Eigen". It implements specific loop unrolling and vectorization algorithms to improve performance of matrix operations, such as (8) on CPUs [31].

The analysis of the transient case, due to the linearity of the process, is reduced to the analysis of a set of CW processes corresponding to the spectral components. For a signal with time discretized into N time points, the number of spectral components in the single-sided discrete Fourier transform is approximately equal to $N/2$ and is therefore quite large (several thousand). However, in practice, the spectrum of an ultrasonic pulse is limited by the transducer frequency band and, therefore, does not contain significant high- and low- frequency components. This simplifies the signal analysis allowing the neglect of high- and low- frequency harmonics whose acoustic power falls below a certain threshold – i.e., by applying band-pass digital filtering. In this case, a set of harmonic components $H_n(\mathbf{r}), n = N_{\min} \dots N_{\max}$ with a frequency step of Δf is used as input data for modeling, resulting in an output set of pressure or velocity $Q_n(\mathbf{r})$, $n = N_{\min} \dots N_{\max}$ .To reconstruct the transient output pulses $q(\mathbf{r}, t_s)$ (q is either pressure or velocity), the IDFT (3) was used for the Rayleigh integral projection results $Q_n(\mathbf{r})$ for each single-frequency component (8):

$$q(\mathbf{r}, t_s) = \sum_{n=N_{\min}}^{N_{\max}} |Q_n| \cos(2\pi f_n t_s + \arg(Q_n)). \qquad (9)$$

In the toolbox, band-pass filtering is applied using the condition that the total power of the hologram spectrum at the maximum frequency is less than 1% of that at the central frequency f_0. Spectral amplitudes V_n outside the frequency range , $N_{\min} < n < N_{\max}$ are considered minor and set to zero. The angular spectrum-based method for power calculation in a single-frequency planar scan, described in detail elsewhere [32], was used. The toolbox includes an option to automatically determine the $N_{\min}$ and $N_{\max}$ values based on the 1% threshold. Alternatively, there is a tool to manually adjust these values, depending on precision requirements.

C. Automatic Alignment of Field Back-Projection to the Surface of a Strongly Focused Transducer

The relative orientation of planar scan and the transducer radiating surface is usually known only approximately. The distance L_H between the transducer surface and the planar scan area (hologram plane) can be calculated with reasonable accuracy based on the time delay of the hydrophone signal. Less certain is the angular alignment of the planar scan (and its corresponding hologram) relative to the ultrasound beam axis (which is usually related to the transducer geometry). This type of misalignment between the z'-axis of the positioning system (mechanical coordinates) and the z-axis of the transducer (acoustical coordinates) is illustrated in Fig. 2(a)). A simple back-projection of the hologram measured in the mechanical coordinates leads to field reconstruction at an incorrect surface (dotted line in Fig. 2(a)).

The methods for fast calculation of the Rayleigh integral described in the previous subsection provide a practical solution to the alignment problem. The solution is based on the idea that the acoustic beam axis can be identified by locating the symmetrical regions of its 3-D pressure amplitude field. For a focused ultrasound source with a diameter much larger than a wavelength and a focal distance comparable to the diameter, such a region exists – it is the focal region, where wave energy is localized within a quasi-ellipsoidal volume (Fig. 3(a)). For such an ellipsoid the axis of symmetry can be considered as the acoustic axis of the transducer. Thus, by reconstructing the field inside the high-amplitude ellipsoid (from the measured hologram), one can uniquely determine the acoustic axis and the location of the focal point. Knowing the acoustic axis, the measured hologram can be projected onto a plane that is perpendicular to and centered on the acoustic axis. Using this new, “aligned hologram” (Fig. 3(b)), it is then possible to use back-projection to accurately reconstruct the vibration velocity patterns on the transducer surface.

The toolbox implements the above algorithm, which is described in more detail below. Since the transducer axis and its position are the same for all frequencies, it is sufficient to use one of the single-frequency holograms. It is convenient to use the transducer's central frequency f_0 for this purpose to optimize the signal-to-noise ratio. In this approach, a single-frequency hologram H_{n_0} (where $f_0 = n_0\Delta f$) is considered as input data.

It is assumed that the transducer has a spherical shape with nominal values for the focal distance F (radius of curvature) as well as the aperture dimensions $D_{\min}$ and $D_{\max}$, which are the minimum and maximum dimensions of the transducer (in the case of a circular transducer, they are equal). In addition, the distance L_H from the center of the transducer to the center of the measured hologram (see Fig. 3(a)) is assumed to be approximately known based on the delay τ_{delay} of the pulse signal when the hydrophone is positioned in the hologram center: $L_{\text{H}} = c_0\tau_{\text{delay}}$. The parameters F, $D_{\min}$, $D_{\max}$ and L_{H} are specified as input data in the toolbox.

$D_{\max}$ is necessary for the proper selection of the diameter of the area on the intended transducer surface where the hologram will be back-projected. The nominal lengths F, $D_{\min}$, and L_{H} are needed to estimate the position and extent of the focal region. Such an estimate can be made based on the well-known idealized model of a uniformly vibrating focused source shaped as a spherical bowl [33]. In this model, the point of maximum pressure is located with high accuracy at the center of curvature of the radiating surface, at a distance equal to its radius of curvature F. The axial distance between the focus and the nearest pre-focal and post-focal nulls is $\Delta z \approx \lambda_0/(1-\cos\theta)$, where $\lambda_0 = c_0/f_0$ is the wavelength, θ is the focusing half-angle, $\sin\theta = D/(2F)$, and D is the source diameter. In the transverse direction, the pressure nulls are located at a distance of $\Delta r \approx 1.22\,\lambda_0 F/D$ from the axis. If the source is not round, but is characterized by two different diameters, $D_{\min}$ and $D_{\max}$, the expressions for Δz and Δr can be used with $D = D_{\min}$.

The automatic alignment is included in the toolbox in the “examples” folder. The algorithm can be broken into several steps:

1) The estimates of the coordinates of the pressure nulls near the focus are calculated as $x_1 = y_1 = -\Delta r$, $x_2 = y_2 = \Delta r$, $z_1 = F - L_H - \Delta z$, and $z_2 = F - L_H + \Delta z$, where Δz and Δr are expressed through λ_0, F, and $D_{\min}$. Assuming that the mechanical and acoustic axes are close to each other, a cuboid region of interest (ROI) in mechanical coordinates is considered: $x_1 - \epsilon_{\text{pos}} < x' < x_2 + \epsilon_{\text{pos}}$, $y_1 - \epsilon_{\text{pos}} < y' < y_2 + \epsilon_{\text{pos}}$, $z_1 - \epsilon_{\text{pos}} < z' < z_2 + \epsilon_{\text{pos}}$. Here ϵ_{pos} is a manually set number representing the expected error in determining the position of the source hologram center relative to the acoustical axis. The recommended default value is $\epsilon_{\text{pos}} = 10\lambda_0$, which implies significant misalignment. Thus, it is assumed that the selected region of interest covers the entire focal region in mechanical coordinates (Fig. 3(a)).

2) The next step is to quickly estimate the boundary of the ellipsoidal-shaped high-amplitude region within the initially selected ROI. For this, the pressure is calculated using a coarse grid within the ROI. The simulation is performed in the mechanical coordinates x', y', z' with the origin O' at the center of the measured hologram (Fig. 3(a)). These simulations involve a forward projection from the hologram $H_{n_0}(x_l', y_k')$, measured within the plane $z' = 0$ and the output is the 3-D pressure amplitude field at the vertices of the coarse simulation grid inside the ROI with steps of Δr_{C} and Δz_{C} in the lateral and axial directions. These grid steps are set in terms of the number of points per wavelength PPW = λ_0/”step”, with the default recommended values being 3 PPW in the lateral directions and 2 PPW in the axial direction. The resulting 3-D field is analyzed to extract an iso-surface of points with equal pressure values p_{level} normalized by the maximum pressure amplitude. In the toolbox, the default level p_{level} = 0.6 is used.

3) After estimating the iso-surface of the high-amplitude volume, the pressure field is calculated again with better spatial resolution. Since this ellipsoidal-shaped region is smaller than the original ROI, finer grid steps can be used to find the wave amplitude distribution in it. The default parameters are 10 PPW in the axial direction and 20 PPW in the radial direction. Note that a larger number of points in the radial direction is required

because the effect of the transducer's rotation on the high-amplitude ellipsoid position is more noticeable in that direction. The solid green contour in Fig. 3(a) shows the fine-grid iso-surface for the high-amplitude region.

4) For transverse cross-sections at each axial position within the ellipsoidal-shaped region the coordinates of the pressure maxima are found. The ordinary least squares method is then used to plot a straight fitting line using these points (Fig. 3(a), red dotted line) [34]. This line represents the acoustical z-axis of the transducer, and its direction unit vector in the mechanical coordinates is denoted as $\mathbf{e}_z$. The point $\mathbf{r}'_{\max} = (x'_{\max}, y'_{\max}, z'_{\max})$ of maximum acoustic pressure amplitude within the high-amplitude volume is denoted by a star in Fig. 3, so the distance between this point and the radiating surface can be found even without using the hydrophone-measured time delay, assuming it to be equal to the nominal focal distance F (in the case of curved radiators, the radius of curvature): hence $\mathbf{r}'_0 = \mathbf{r}'_{\max} - F \cdot \mathbf{e}_z$.

5) After the acoustic z-axis unit vector $\mathbf{e}_z$ is specified, the directions of the x-and y-axes – the acoustic coordinates – are determined. It is convenient to determine $\mathbf{e}_x$ and $\mathbf{e}_y$ using the following expressions: $\mathbf{e}_x = \mathbf{e}'_y \times \mathbf{e}_z / |\mathbf{e}'_y \times \mathbf{e}_z|$ and $\mathbf{e}_y = \mathbf{e}_z \times \mathbf{e}_x$, where $\times$ and $|\cdot|$ denote the vector product and the absolute value of a vector, and $\mathbf{e}'_x = (1, 0, 0)$, $\mathbf{e}'_y = (0, 1, 0)$, and $\mathbf{e}'_z = (0, 0, 1)$ are the unit vectors of the mechanical coordinate system (presented in the same system).

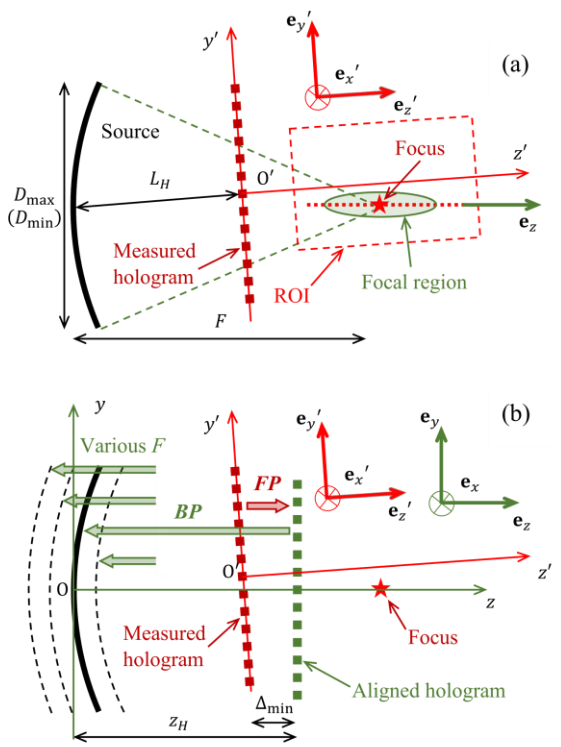

Fig. 3. Schematics illustrating the automatic alignment algorithm: (a) initial steps involve using the measured hologram to calculate the 3-D acoustic pressure distribution in the region of interest (ROI) and using this data to find the focal point and the axis of symmetry of the transducer (acoustical axis); (b) subsequent steps involve forward projection (FP) of the measured hologram onto an auxiliary hologram centered on and oriented perpendicular to the acoustic axis, and then back-projection (BP) of the field from this new hologram onto a series of concentric segments of spherical surfaces with the center of curvature at the focal point, to find the normal velocity distribution on the radiating surface.

6) After determining the acoustic coordinate system, the measured hologram is transferred to an auxiliary hologram specified on a flat section of the same size in the transverse plane (x, y) of the acoustic coordinate system. The region of the new hologram is chosen close to that of the original hologram, so that the distance between the closest points of the two holograms is several wavelengths. The rationale for this choice is as follows. As shown in prior work [8], the calculation of the Rayleigh integral based on the discretized pressure differs from the exact value only within a distance of the order of a wavelength from the integration surface. This is because the difference between the exact and the numerical results has the form of evanescent waves that quickly fade with distance from the surface. By default, the minimum distance $\Delta_{\min}$ between the two holograms is chosen equal to 4 wavelengths: $\Delta_{\min} = 4\lambda_0$.

To define the plane of a new hologram, first consider the position vector of a point on the original hologram region: $\mathbf{r}' = x'\mathbf{e}'_x + y'\mathbf{e}'_y$. Denote a position vector of a point with the largest value of acoustical coordinate z as $\mathbf{r}'_* = x'_*\mathbf{e}'_x + y_*{}'\mathbf{e}'_y$. The position vector of the same point in the acoustic coordinate system is $\mathbf{r} = \mathbf{r}'_* - \mathbf{r}'_0 = F\mathbf{e}_z + \mathbf{r}'_* - \mathbf{r}'_{\max}$. The acoustic z-coordinate of the point is then $z_* = \mathbf{r} \cdot \mathbf{e}_z = F + (x'_* - x'_{\max})(\mathbf{e}'_x \cdot \mathbf{e}_z) + (y'_* - y'_{\max})(\mathbf{e}'_y \cdot \mathbf{e}_z) - z'_{\max}(\mathbf{e}'_z \cdot \mathbf{e}_z)$. The aligned hologram acoustic z-coordinate is chosen as $z_H = z_* + \Delta_{\min}$. Thus, the aligned hologram is located prefocally at a distance from the focus equal to $\Delta_H = F - z_H = (x'_{\max} - x'_*)(\mathbf{e}'_x \cdot \mathbf{e}_z) + (y'_{\max} - y'_*)(\mathbf{e}'_y \cdot \mathbf{e}_z) + z'_{\max}(\mathbf{e}'_z \cdot \mathbf{e}_z) - \Delta_{\min}$.

To perform forward projection from the original hologram H_{n_0} to the aligned one $H^A_{n_0}$, it is necessary to know the mechanical coordinates $\mathbf{r}'_{qs} = (x'_{qs}, y'_{qs}, z'_{qs})$ of the grid points of the new hologram. The radius-vectors of these points in acoustic coordinates are $\mathbf{r}_{qs} = x_q\mathbf{e}_x + y_s\mathbf{e}_y + z_H\mathbf{e}_z$, $x_q = [q - (L+1)/2]\,\Delta x_H$, $y_s = [s - (M+1)/2]\,\Delta y_H$ with $q = 1, \ldots, L$ and $s = 1, \ldots, M$. If $\mathbf{r}'_{qs}$ is the position vector measured from the origin of the mechanical coordinate system, then $\mathbf{r}'_{qs} = \mathbf{r}'_0 + \mathbf{r}_{qs} = \mathbf{r}'_{\max} - F \cdot \mathbf{e}_z + \mathbf{r}_{qs}$. In the mechanical coordinate system $\mathbf{r}'_{qs} = x'_{qs}\mathbf{e}'_x + y'_{qs}\mathbf{e}'_y + z'_{qs}\mathbf{e}'_z$, and thus $x'_{qs} = x'_{\max} - \Delta_H(\mathbf{e}_z \cdot \mathbf{e}'_x) + x_q(\mathbf{e}_x \cdot \mathbf{e}'_x) + y_s(\mathbf{e}_y \cdot \mathbf{e}'_x)$, $y'_{qs} = y'_{\max} - \Delta_H(\mathbf{e}_z \cdot \mathbf{e}'_y) + x_q(\mathbf{e}_x \cdot \mathbf{e}'_y) + y_s(\mathbf{e}_y \cdot \mathbf{e}'_y)$, and $z'_{qs} = z'_{\max} - \Delta_H(\mathbf{e}_z \cdot \mathbf{e}'_z) + x_q(\mathbf{e}_x \cdot \mathbf{e}'_z) + y_s(\mathbf{e}_y \cdot \mathbf{e}'_z)$, where $\Delta_H = F - z_H$. Once the location of the aligned hologram is found, this new hologram $H^A_{n_0}$ is calculated from the original hologram H_{n_0} using FP from pressure to pressure.

7) In the last step, the aligned hologram is back-projected onto the transducer surface (Fig. 3(b), green ***BP*** arrows) to calculate the complex amplitude $V_{n_0}(\mathbf{r})$ of the normal component of the vibrational velocity. Unlike the previous steps, this back-projection is performed using acoustic

coordinates based on the pressure complex amplitude $H_{n_0}^A$ at the grid points $\mathbf{r}_{qs} = (x_q, y_s, z_H)$.

The GUI of the script allows changing the nominal radius of curvature F and repeating the back-projection to find the effective value F_{eff}, which represents the true transducer geometry (Fig. 3(b), dashed arcs). The position of the radiating surface can be corrected by repeating the back-projection for different F values to find the position at which the details of the vibrating surface are most clearly defined. The back-projected vibrational velocity distribution $V_{n_0}(\mathbf{r})$ and the alignment parameters can be saved for further simulations.

Note that the presented steps of the algorithm are performed completely automatically without any intermediate actions required from the user.

In addition to the automatic hologram repositioning for a strongly focused transducer in CW (*i.e.*, single frequency) mode, the toolbox also includes an automatic alignment script for a more general transient situation. Since the alignment parameters are the same for all harmonic components, the transient alignment script uses the predefined alignment parameters saved from the single frequency alignment script. Therefore, when analyzing a transient hologram, steps 1–6 described earlier in this section are the same – the acoustic coordinate system is adjusted using the CW hologram at the center frequency. As for steps 7 and 8, they are performed by the same forward and backward projection procedures, but in the transient regime. The results are presented both in the frequency domain as a set of complex amplitudes V_n, $n = 1 \dots N_{\max}$, and in the time domain $v(\mathbf{r}, t_s)$, $s = 1 \dots N-1$ using the IDFT given by (9).

D. Manual Alignment of Field Back-Projection to the Transducer Surface

The automated alignment algorithm described in Section II-C utilized the characteristics of fields radiated by strongly focused transducers to infer the position and orientation of the transducer from the structure of the acoustic field. This approach succeeds for two reasons: first, the acoustic field unambiguously specifies the position of the surface curvature center as the point of maximum wave amplitude; second, the acoustic axis is readily identified as the symmetry axis of the focal region. However, in many cases without strong focusing, such automation is challenging. For instance, when the diameter of the focused source is not larger than the wavelength, the point of maximum amplitude shifts noticeably from the center of curvature towards the transducer. Therefore, determining the position of the radiating surface requires selecting not only the radius of curvature, but also the position of the center of curvature, which complicates the process. Another example is flat sources. Although they do not have a focal point, there are diffraction maxima in the near field, that can be used to identify the acoustical z-axis.

Finding the acoustic axis and the transducer surface is additionally complicated if the source is not axisymmetric – e.g., when part of its surface is damaged and does not radiate. In these cases, the acoustic axis and the relative position of the transducer can still be determined interactively based on a visual analysis of the 3-D field structure and setting the direction of the acoustic axis $\mathbf{e}_z$ by slecting two points with mechanical coordinates $\mathbf{r}_1' = (x_1', y_1', z_1')$ and $\mathbf{r}_2' = (x_2', y_2', z_2')$, $z_2' > z_1'$, as $\mathbf{e}_z = (\mathbf{r}_2' - \mathbf{r}_1')/|\mathbf{r}_2' - \mathbf{r}_1'|$. For example, these points can be points on the field symmetry axis or on the projection of the field onto the nominal surface of the source and the point of maximum or minimum of the field at some distance from the transducer. The distance from the selected point to the source can be calculated based on the delay in the arrival of the pulse signal at the reference point. The toolbox provides options to assist in the manual determination of transducer alignment along with implementation of this alignment for field reconstruction on the transducer surface.

E. Implementation and Interface for the xDDx Toolbox

The expressions presented in Section II-B were implemented in the xDDx toolbox. The toolbox was developed in MATLAB and includes both a scripting interface and a graphical user interface (GUI) as a wrapper around the C++. A comprehensive technical explanation of the interface features is given in the software documentation [30]. This section only highlights the general features of the toolbox.

The core of xDDx is a universal function applicable for forward/backward projection in transient or single-frequency holography mode. The first mode reconstructs a set of harmonic components $Q_n(\mathbf{r}), n = 1 \dots N_{\max}$ and the second reconstructs a single harmonic component $Q_{n_0}(\mathbf{r})$ at $f_0 = n_0 \Delta f$.

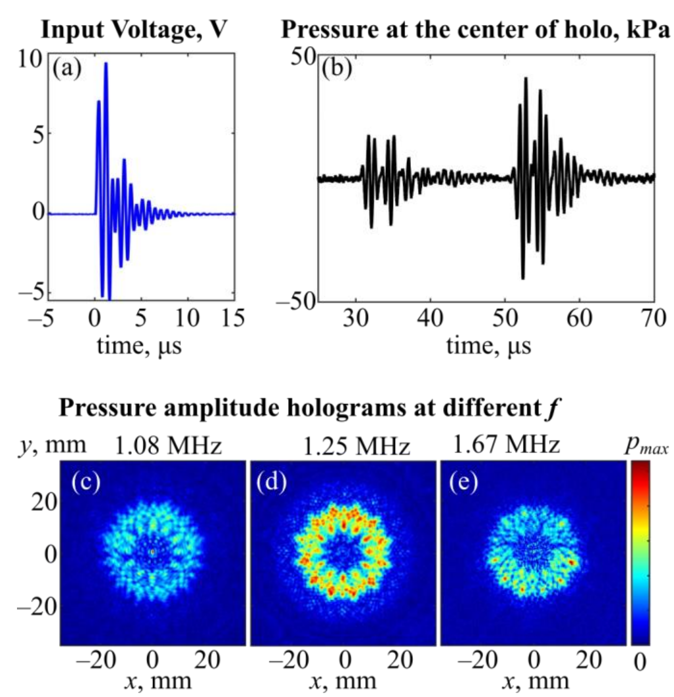

Fig. 4. (a) Voltage signal at one of the elements of the strongly focused transducer used for holography and (b) the hydrophone-measured pressure signal at the center of the hologram. Spectral magnitudes of the pressure in the hologram at different frequencies (c – e).

This function operates in six regimes that identify forward/backward projections (FP/BP) with specific pressure/velocity (P/V) inputs and outputs.

- Regime 1: BP of the input P at a flat surface to calculate output V at a flat surface.
- Regime 2: BP of P (flat) to V at a spherical surface.
- Regime 3: FP of V (sphere) to P at an arbitrary set of points.
- Regime 4: FP of V (flat) to P (arbitrary).
- Regime 5: FP of P (flat) to P (arbitrary).
- Regime 6: BP of V (sphere) to P (flat).

xDDx tools are presented as separate MATLAB/Octave scripts that call the core function one or more times to perform simulations and display the results. For example, the automatic hologram alignment (Section II-C) includes Regime 5 for focal lobe detection and planar scan repositioning, and Regime 2 for back-projection at the transducer surface. Other xDDx tools combine Regimes 1 – 6 to simulate the field radiated by user-defined transducers with the boundary conditions set for pressure or velocity. Even though the existing tools cover many needs for transducer diagnostics and field simulation, users can create their own tools based on the existing scripts and simulation regimes to address specific cases.

F. Experimental Arrangement and Set-Up for Sample Experiments for Toolbox Demonstration

Two focused transducers were used for the demonstration of xDDx toolbox capabilities. Each of these custom-built transducers was constructed using 12 flat piezoelectric elements (Fig 1). The ultrasound fields from these elements were focused to the same point by 3-D-printed plastic lenses [35].

Both transducers were designed for histotripsy and shared the following specifications: nominal aperture of $D = 87$ mm, nominal central opening aperture of $O = 40$ mm, and operating frequency of $f_0 = 1.25$ MHz. The first transducer, termed “Transducer 1,” had a focal distance of $F = 65$ mm, while the other, termed “Transducer 2,” had a focal distance of $F = 87$ mm (corresponding to F-numbers $= F/D$ of 0.75 and 1, respectively). The transducer elements were driven in phase using a custom-built class D amplifier [24].

Each transducer was submerged in a tank filled with degassed and deionized water. A 3-D positioning system (Velmex Inc., Bloomfield, NY) was employed to position an HGL-0200 capsule hydrophone. The hydrophone signal was sent to an AH-2020 preamplifier set at 20 dB gain (Onda Corp., Sunnyvale, CA), which was connected to a 14-bit digitizer (Gage Razor 14, DynamicSignals LLC, Lockport, IL, USA). The hydrophone motion and signal acquisition were controlled with a custom LabVIEW program (National Instruments Corp., Austin, TX). The program coordinated a hydrophone planar scan over a grid of 177 × 177 points with a step size of $\Delta x_H = \Delta y_H = 0.4$ mm. This step size provides 3 grid points per wavelength at a frequency $f_0 = 1.25$ MHz (given an estimated sound speed of 1500 m/s), which is a reliable spacing for transient holography [7, 21]. The hydrophone signal was sampled every $\Delta t = 12.5$ ns, and the total number of time points per waveform was $N = 6000$.

Fig. 4(a) shows an input voltage waveform applied to each element of the Transducer 1 for holography measurements. The central frequency of the pulse matched the operating frequency of the transducer, and the excitation burst was 2 cycles in duration, with a pulse repetition frequency (PRF) of 20 Hz.

The position of the center of the scan ($z' = 0$ in Fig. 2 and 3) was manually selected to coincide with the center of symmetry of the field in the scan plane, approximately at $L_H = 45$ mm distance from the apex for Transducer 1 and $L_H = 55$ mm for Transducer 2. This position falls within 0.5 – 0.7 of the nominal focal distance, which has been shown to be reasonable for acoustic holography [8]. The position L_H was calculated based on the time delay τ_{delay} of the signals recorded at the center of the holograms: $L_H = c_0 \tau_{\text{delay}}$. It is important to note that due to imperfect alignment, the axis of symmetry of the transducer, z, was not explicitly aligned with the axes of the 3-D positioner, z' (Fig. 2(a)).

The positions and sizes of scan regions were chosen to capture the entire field of the transducers. A useful empirical rule is to ensure that peak pressure levels at the edge of the region are less than 5% of the maximum value in the holography scan. The transducer was excited by repetitive pulses, and waveforms recorded by the hydrophone at each hologram point were averaged during acquisition (16 averages per point, to minimize inherent noise) and saved to a binary file for post-processing.

An example of a recorded pressure pulse $p_{\text{H}}(x_l{}' = 0, y_m{}' = 0, t_s)$ at the center of the hologram is shown in Fig. 4(b). Examples of xy distributions of the absolute values of single-frequency hologram components $|H_n|$ are shown in Fig. 4(c – e) for three frequencies $f_n = 1.08$, 1.25, and 1.67 MHz.

G. Toolbox Validation

The holography method implemented in this toolbox inherently involves approximations related to discretization of the field. As shown in [8], errors associated with the radiated field are expected to remain small (< 1%) when proper discretization choices are made. To validate the performance of the xDDx toolbox under practical conditions, here we considered the field radiated by an idealized transducer through the following steps:

(1) A spherically focused transducer vibrating as a uniform piston was defined with the same operating frequency and geometry as Transducer 1 from Section II-F, considering radiation into water (sound speed $c_0 = 1500$ m/s, density $\rho_0 = 1000$ kg/m^3) and a vibrational velocity amplitude V_I chosen such that the characteristic surface pressure $\rho_0 c_0 V_I = 1$ Pa.

(2) The radiated field was calculated with xDDx toolbox in two transverse planes with different orientations to simulate measured holograms. The holograms’ orientations and grid steps were chosen to match those used in the real transducer case (Fig. 3(b)) described in Section II-F. Of the two simulated hologram orientations, one was perfectly aligned and centered relative to the transducer and the other was misaligned, with a 9.1-mm shift and a 2.3° rotation relative to the transducer.

(3) Backward projections from the holograms were used to reconstruct the vibrations on the transducer surface to enable

comparison to the idealized source. The misaligned hologram was then aligned using the xDDx automatic alignment algorithm.

(4) The reconstructed sources were used to perform an on-axis projection of the radiated field for comparison against an analytical solution [33].

III. Results

A. Simple Back-Projection with No Alignment

This section demonstrates the importance of hologram alignment using Transducer 1 as an example. To illustrate this, BP was performed assuming that the acoustic and mechanical axes were aligned (i.e., coincident). The measured hologram H_{n_0} was used as input for Step 7, described in Section II-C. Fig. 2(b, c) show the BP results: the amplitude $|V_{n_0}| \equiv |V_0|$ and phase $\arg(V_0)$ of the vibrational velocity at the spherical surface of the transducer.

The output spatial region (x/y/z grid) for V_0 was chosen to capture the entire transducer aperture. The output 201×201 grid was located at the spherical surface of the transducer: $V_0(x_r = r \cdot \Delta x_S,\ y_q = q \cdot \Delta y_S,\ z_{rq})$, where $r,\ q = -100, \ldots, 100$, $\Delta x_S = \Delta y_S = 0.5$ mm, $z_{rq} = F - \sqrt{F^2 - x_r^2 - y_q^2}$, $F = 65$ mm was the nominal radius of curvature. To reduce the number of simulation points, the set of the output matrix points $(x_r, x_q,\ z_{rq})$ was considered inside the nominal transducer aperture D, in other words, the condition $x_r^2 + y_q^2 \leq (0.5D)^2$ was fulfilled. The final number of output points within the aperture circle was 23757.

The amplitude plot in Fig. 2(b) demonstrates a distinguishable pattern of 12 elements, which is, however, imprecise due to the imperfect alignment of the mechanical and acoustical axes. Specifically, the gaps between the elements have nonzero amplitudes, and the edges of the transducer do not oscillate, indicating that the reconstruction surface is closer to the focus than the actual surface, and thus the reconstructed field is slightly narrowed due to focusing.

The rotational misalignment between the mechanical and acoustic axes is clearly demonstrated in the phase distribution (Fig. 2(c)). The phase at the surface of spherically shaped transducers should be uniform to provide high focusing quality. However, the obtained distribution has a striped structure, clearly indicating the rotation of the reconstruction surface (Fig. 2(a), dotted arc). Therefore, the obtained mismatched

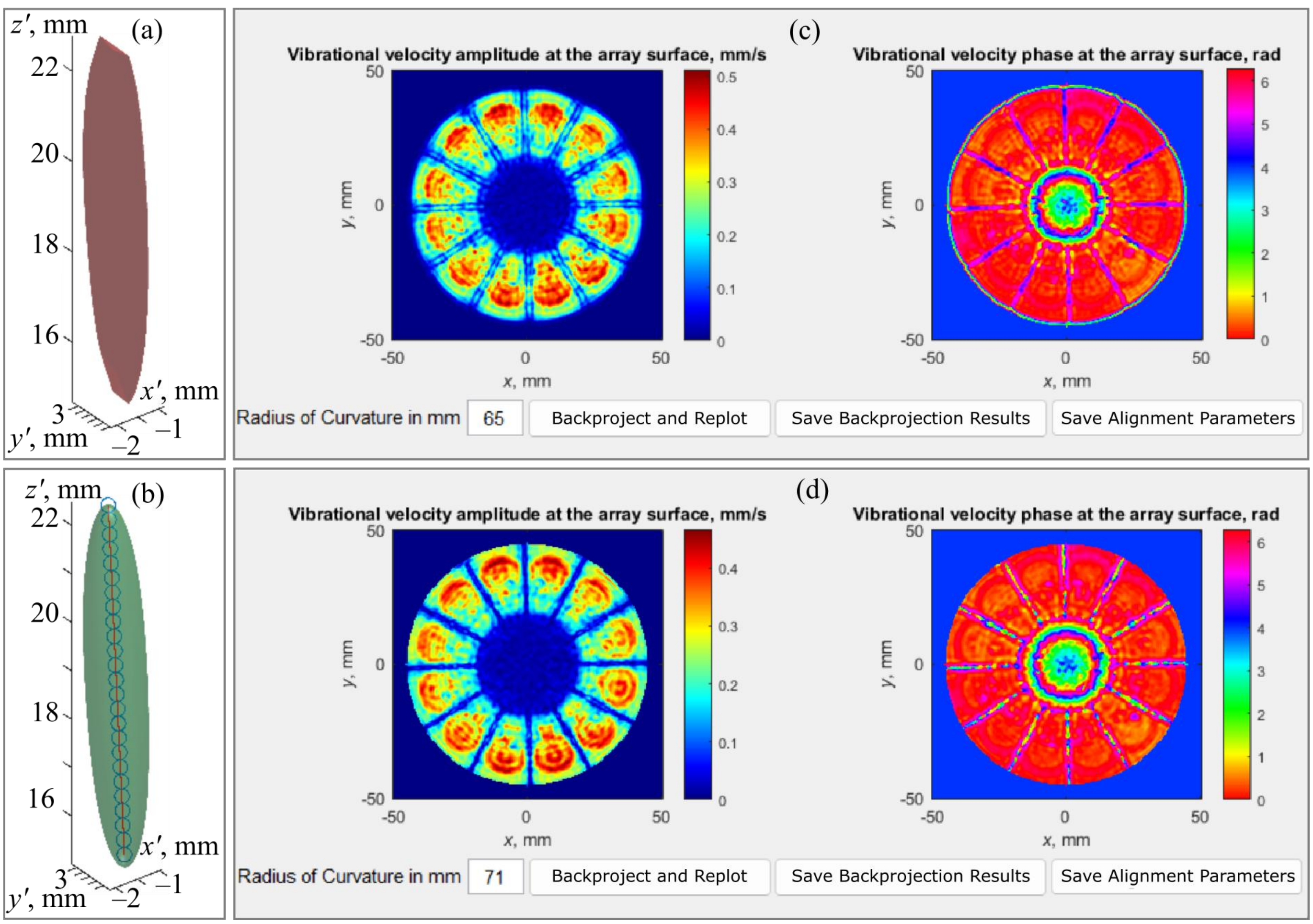

Fig. 5. Results of the automatic alignment for Transducer 1: coarse-grid (a) and fine-grid (b) simulations of the focal lobe shape. GUI windows with the back-projection results after alignment for the nominal radius of curvature of F = 65 mm (c) and the determined effective radius of curvature of F = 71 mm (d).

phase distribution does not provide information on phase uniformity at the transducer surface.

B. Automatic Alignment for Single Frequency

The same Transducer 1 case was used to demonstrate the performance of the automatic alignment script in the single-frequency case. The results at different stages of the alignment process are summarized in Fig. 5. Below, we describe this process, referring to the Automatic Alignment Algorithm Steps (Section II-C).

Fig. 5(a) presents the result of the first coarse-grid simulation of the focal lobe (Step 2) at the default iso-level $p_{\text{level}} = 0.6$. The plot in the mechanical coordinates (x', y', z') shows slight rotation of the mechanical axes relative to the acoustic axes.

The fine-grid 3-D simulation (Step 3) refines the shape of the focal region (Fig. 5(b)) and provides the position of the center of curvature $x'_{\max} = -1.5$ mm, $y'_{\max} = 2.7$ mm, and $z'_{\max} = 18.6$ mm (Step 4 in Section II-C). The solid line passing through the circular markers (Fig. 5(b)) provides the ordinary least squares-estimated direction of the acoustic axis of the transducer (direction vector $\mathbf{e}_z$) and reveals a rotation angle between the acoustic and mechanical axes of 2.3°. Note that rotations of approximately 1°, along with the displacements of approximately 1 mm ($x'_{\max} = -1.5$ mm, $y'_{\max} = 2.7$ mm), are typical for manual assembly of an experimental setup.

Fig. 5(c) shows the back-projection result obtained at Steps 7 and 8 of the algorithm described in Section II-C. The GUI window presents the amplitude and phase distributions in a manner similar to the one described in Section III-A. The edit field labeled “Radius of Curvature in mm”, contains the nominal value $F = 65$ mm. This value can be changed, and the BP can be repeated using the button “Backproject and Replot”. Two other buttons can be used to save the back-projected vibrational velocity distribution and the alignment parameters, respectively.

The amplitude distribution obtained for the nominal radius of curvature is close to that of the Simple Back-Projection case (Section III-A), however, the phase distribution is noticeably different.

After alignment, the phase distribution is mostly uniform, with the exception of minor local defects caused by the 3-D-printed lens manufacturing. As discussed above, the nominal radius of curvature was shorter than the actual one. Using the GUI, it was adjusted several times to find the effective value F_{eff}. The process of determining this value is analogous to bringing an optical image into focus: the appropriate value of F will result in matching the reconstruction and the real transducer surfaces and will provide the sharpest distribution (“image”). In the considered case, this sharpening process resulted in the value $F_{\text{eff}} = 71$ mm (Fig. 5(d)). The distribution of the vibrational velocity amplitude was significantly improved: the contours of the elements and the gaps between them became sharper. The phase distribution remained almost identical to the case of nominal F (Fig. 5(d)) because the shape of the wavefront generated by the array remained spherical. To avoid constant phase shifts between the focus-sharpening cases, that can affect the relative analysis of the phase

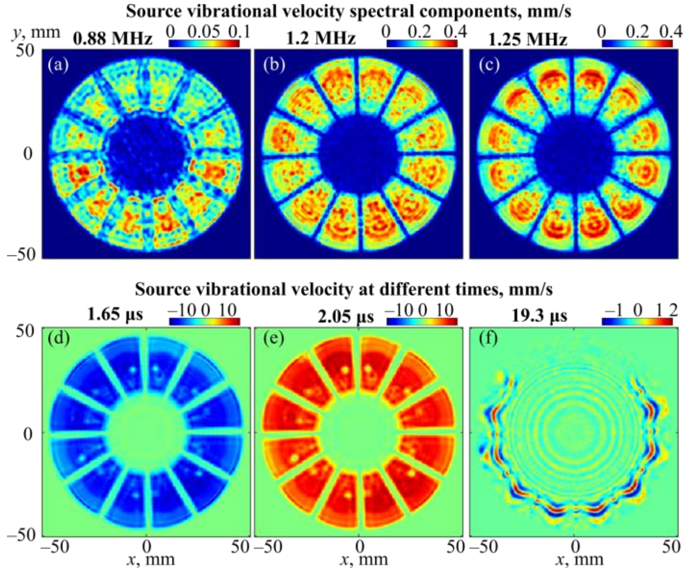

Fig. 6. Back-projection results after alignment in the transient case are shown in the frequency domain (a-c) for different transducer frequencies and in the time domain (d-f) for different time moments. The example is shown for Transducer 1.

distributions, the phases in Fig. 5(c, d) are set to zero at a specific point of the transducer aperture $x = y = -25$ mm and the phases are wrapped to 2π. Other coordinates of zero phase can be selected in the script if needed.

An important detail of the BP results above is that even though the array elements oscillate as uniform pistons, the obtained amplitude distribution (Fig. 5(d)) is not uniform due to Lamb waves that propagate along the surface of the elements and manifest themselves in continuous wave (CW) regimes (including the single-frequency regime considered here) by affecting locally the vibrational velocity of the plates [36, 37].

C. Automatic Alignment for a Transient Hologram Case

Fig. 6 shows a compilation of BP with automatic alignment in the transient case. The BP results were obtained at the vertices of the same spatial simulation grid $(x_r, y_q,\ z_{rq})$ as for the single-frequency cases in the two previous subsections. Two representations of the results are shown, one in the frequency domain and one in the time domain.

The top row of Fig. 6 shows the frequency domain results as a set of normal velocity complex amplitude distributions $V_n(x_r, y_q,\ z_{rq})$, $n = N_{\min} \dots N_{\max}$. To fulfill the 1% requirement (Section II-B) in the considered case given the frequency step $\Delta f = (N \cdot \Delta t)^{-1} = 13$ kHz, the maximum number of frequencies was set to $N_{\max} = 200$. The minimum frequency sample was set to $N_{\min} = 1$ which fulfilled the 1% requirement and excluded the constant zero-frequency component.

Three frequency samples from this set are shown in Fig. 6(a–c). The low-frequency mode of 0.88 MHz (Fig. 6(a)) results in a noisy and nonuniform vibrational velocity amplitude pattern, as the thickness of the piezoelectric elements does not support this frequency. However, the frequency of 1.2 MHz (Fig. 6(b)) demonstrates better performance compared to the nominal frequency of $f_0 = 1.25$ MHz (Fig. 6(c)). The amplitude distribution for 1.2 MHz is more uniform than that for 1.25

MHz, which allows more effective usage of the active surface of the array in CW therapeutic regimes.

The bottom row of Fig. 6 presents the time domain results $v(\mathbf{r}, t_s)$ at three different time points. For convenience, the zero time here corresponds to the beginning of the signal, when the surface amplitude first surpassed 10% of the maximum. The significant advantage of time domain images for short transient pulses is that the Lamb waves do not manifest themselves as they do in CW regimes, allowing for visualization of small-scale surface defects and geometrical details of the radiating surface. Figs. 6(d – e) show 2D velocity distributions at the surface for $t_s = 1.65$ and 2.05 μs, respectively. These time samples correspond to reaching the minimum and maximum vibrational velocity respectively at the reconstructed surface through the entire signal duration. The small-scale details of the transducer can be seen here, such as wiring solder points at each element and a slight velocity decrease at the edges of some elements. The last time point shown in Fig. 6(f) demonstrates a surface wave that was generated on the lens of the transducer significantly later ($t_s = 19.3$ μs) than the main piston pulse (Fig. 6(d–e)). Even though the peak velocity of the surface wave is more than five times lower compared to that of the piston pulse, it reveals an important defect of the transducer lens: the circular oscillation pattern in Fig. 6(f) is not closed, which could indicate incomplete lens attachment. The frequency and time domain results are available in the supplementary materials as movies where each frequency/time sample corresponds to a specific frame (Supplement videos 1 and 2). This allows for a closer examination of the radiating surface details.

D. Manual Alignment for an Asymmetric Beam

The Transducer 2 case, which was a representative example of semi-manual defect detection, is considered here.

Steps 2–3 of the Automatic Alignment Algorithm (Section II-C) resulted in a deformed and split focal lobe shape, which is illustrated in Fig. 7(a) by two iso-surfaces at iso-levels of $p_{\text{level}} = 0.8$ and 0.5. The automatic fitting line could not be plotted in this case due to the asymmetry of the focal lobe. Therefore, in this case the line was plotted manually to estimate the expected direction $\mathbf{e}_z$ of the acoustic axis (Fig. 7(a), dashed arrow) and the position of the center of curvature $\mathbf{r}_{\max}$ (Fig. 7(a), dot marker). After the BP, the distributions of the vibrational velocity amplitude and phase (Fig. 7(b) and (c), respectively) at the central frequency of $f_0 = 1.25$ MHz were obtained. The amplitude pattern shows no significant difference between the array elements, demonstrating that all elements are active. However, the phase distribution clearly shows that four elements have an inverted phase π relative to the other elements, which means that the polarity of the driving wires for positive and negative electrodes for those elements had been inverted during the transducer assembly. This issue could be solved by applying half-cycle phase delays of $-\pi$ to these three elements, which would bring the array performance back to normal.

E. Simulating the 3-D Transducer Field

The last figure, Fig. 7(d), demonstrates another capability of the toolbox: simulation of the 3-D field of a spherically shaped transducer (Regime 3, Section II-E). The back-projected amplitude $V_0(x_r, y_q, z_{rq})$ and phase Fig. 7 (b and c) at the spherical surface of the source were used as a boundary condition to calculate the 3-D field in a wide spatial region ($-45\text{ mm} < x < 45\text{ mm}$, $-45\text{ mm} < y < 45\text{ mm}$, $20\text{ mm} < z < 110\text{ mm}$), with a spatial step of 0.4 mm in all directions (output grid size was $226 \times 226 \times 226$). The results are presented as iso-surfaces corresponding to three iso-levels $p_{\text{level}} = 0.8$, 0.5, and 0.05. This kind of fine-grid simulation in wide spatial regions helps examine the levels of grating or side lobes outside the target region, which can be important for safety. Once this simulation is done for a transducer, it provides comprehensive information about its entire pressure field in 3-D at a frequency of interest.

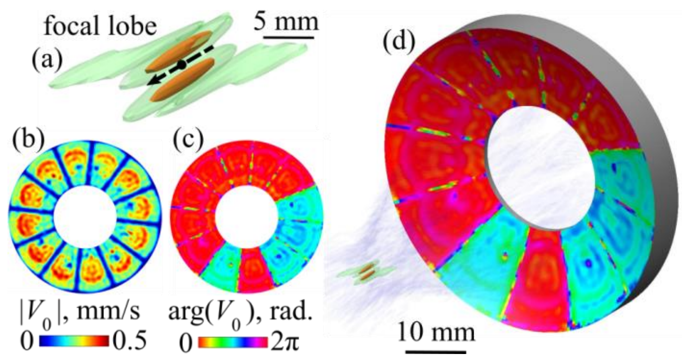

Fig. 7. Semi-manual alignment for an asymmetric beam radiated by a transducer with an aperture and focal distance of 87 mm (Transducer 2), operating at a frequency of $f_0 = 1.25$ MHz. Part (a) shows the pressure amplitude iso-surface levels at 80% and 50% relative to the maximum for the 3-D field projected from the measured hologram. The dashed line indicates the manually selected axis of symmetry. Parts (b) and (c) display the amplitude and phase distributions of the vibrational velocity V_0 at the surface of the transducer obtained after alignment. Part (d) presents iso-surfaces for the entire transducer field simulated using the back-projection results as a boundary condition.

F. Simulation Speed

This section reports simulation speed values for different hardware configurations. Three types of CPU+GPU combinations were considered and sorted into three types based

TABLE I
SIMULATION TIME FOR DIFFERENT DEVISES AND REGIMES

	SBP	ARBS	ARBT	3DE
Graphical cards (GPUs)				
RTX 4090	0.21 s	0.89 s	51 s	14 s
RTX 3070	0.42 s	1.2 s	3.4 min	50 s
GTX 1650	1 s	3.8 s	9.8 min	2.9 min
Central processors (CPUs)				
AMD 7950X3D	1.6 s	14 s	11 min	8.7 min
AMD 5800X	3.2 s	33 s	24 min	20 min
Intel 6700K	8.3 s	1.3 min	57 min	46 min

SBP = Simple Back-Projection, 31329 input points, 23757 output points (Section III-A)
ARBS = Automatic Rotation and Back-Projection for Single Frequency, 31329 input points, 23757 output points (Section III-B)
ARBT = Automatic Rotation and Back-Projection for Transient, 31329 input points, 23757 output points, 200 frequency samples (Section III-C)
3DE = 3-D simulation of entire transducer field, 23757 input points, 11543176 output points (Section III-E)

on the release year of the components:

- Type 1: CPU – AMD Ryzen 9 7950X3D, 16 cores at 4.2 GHz, released in 2023; GPU– NVIDIA GeForce RTX 4090, released in 2022
- Type 2: CPU – AMD Ryzen 7 5800X, 8 cores at 3.8 GHz (2020); GPU – NVIDIA GeForce RTX 3070 (2020)
- Type 3: CPU – Intel Core i7-6700K (Skylake), 4 cores at 4 GHz (2015); GPU – NVIDIA GeForce GTX 1650 (2019)

All configurations presented here are personal computers (PCs) assembled from common components and are not intended for use as workstations for specific resource-intensive applications.

Table I summarizes simulation performance in four simulation cases, described in Section III of this study. The results obtained with GPUs and CPUs are separated into different sections of the table. In all cases, the performance of GPUs was noticeably superior to that of CPUs, even when comparing the Type 3 GPU (GTX 1650, released in 2019) with the Type 1 CPU (AMD Ryzen 9, released in 2022). Single-Frequency Back-Projection and Automatic Alignment simulations (SBP and ARBS in Table I) can be performed in near real-time with all presented GPUs: the simulation time does not exceed 4 s. Transient alignment and 3-D simulation of the array field (ARBT and 3DE in Table I) are significantly more time-consuming, but, their simulation time still fall within reasonable ranges of 14 s – 10 min for GPUs and 9 – 57 min for CPUs.

G. Toolbox Validation

Fig. 8(a) shows the back-projection results of the "perfectly aligned" hologram to reconstruct the vibrational velocity of the idealized source. While the edges of the reconstructed transducer are sharp and the vibrating surface converges to the expected velocity, there is some nonuniformity. This nonuniformity arises from the incorrect reconstruction of evanescent waves. Such behavior is expected from a back-projection of the field based on the Rayleigh integral, which treats the evanescent waves as decaying and, as a consequence, suppresses them [8].

To assess the performance of the automatic alignment algorithm in xDDx, Fig. 8(b) shows the difference in reconstructed surface velocities based on the “perfectly aligned” and misaligned holograms (after alignment using the xDDx toolbox). This reconstruction error E is expressed as a percentage relative to the characteristic surface pressure of the idealized transducer, $\rho_0 c_0 V_I$ = 1 Pa.

The results demonstrate that the surface distributions are not perfectly aligned at the edges of the transducer, where the error reaches values up to 12%. The difference between the two reconstructed velocity distributions is more evident in Figs. 8(c, d), which show 1D velocity distributions and the corresponding error E along the x-direction for y = 0 (Fig. 8(a), dashed line). These figures indicate that the largest errors occur near the edges of the transducer (within approximately 2.5 mm), while in the central region the error E was less than 3%. This error is attributed to two factors:

1) The focal lobe shape simulated during automatic alignment does not provide the exact direction for the acoustic axis due to the finite precision of the 3D simulation grid.
2) The assumption inherent in the automatic alignment that the center of curvature coincides with the pressure maximum of the focused field. While this assumption is reasonable for the strongly focused transducer considered here, it is still an approximation. This limitation is discussed in detail in the discussion section.

Fig. 8(e) illustrates the axial pressure amplitude obtained via forward projections of the reconstructed vibrational velocity distributions for both the perfectly aligned (dashed line) and automatically aligned (dashed-dotted line) holograms. These are compared to the analytical solution for the idealized piston transducer (solid line). The difference between the analytical solution and calculations based on the aligned hologram is negligible, with the maximum amplitude difference being less than 0.02%. Even though evanescent waves affect small details in the velocity distribution of the reconstructed source, these details are not important in the region of interest because evanescent waves decay almost completely within a few millimeters from the transducer surface. The result for the automatically aligned case shows a 0.2-mm shift in the distribution, caused by the automatic alignment assumption that the center of curvature coincides with the pressure

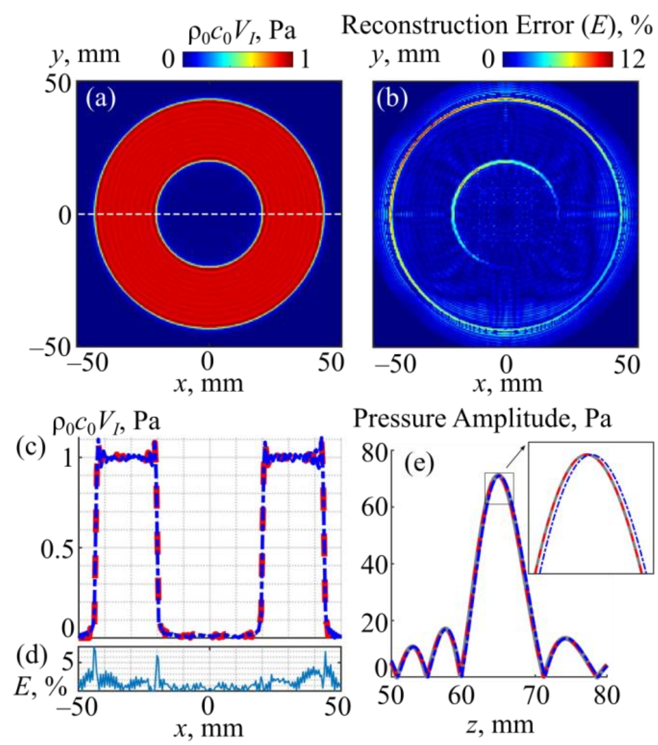

Fig. 8. (a) The vibrational velocity V_I, back-projected to the surface of the idealized transducer from the perfectly aligned hologram. (b) The difference between the surface vibrational velocity reconstructed from the perfectly aligned hologram and that reconstructed from originally misaligned and then automatically aligned hologram. Reconstructed 1D velocity distributions (c) and their percent difference E (d) for the perfectly aligned (dashed line), and automatically aligned (dash-dotted line) holograms. (e) Axial pressure amplitude distribution obtained by forward projection of the perfectly aligned (dashed line) and automatically aligned (dashed-dotted line) holograms compared to the analytical solution for the idealized transducer (solid line).

maximum. Nonetheless, the error in the maximum pressure amplitude for this case relative to the analytical solution is negligible at 0.01%.

IV. Discussion and Conclusions

The xDDx toolbox presented in this paper is designed to facilitate the use of planar scan hydrophone measurements to characterize the 3-D fields radiated by ultrasound transducers in water and to provide diagnostic information about the vibrations at the transducer surface. These capabilities fundamentally rely on accelerated numerical computations of the Rayleigh integral to reconstruct the full 3-D field from holograms defined on flat or spherically curved surfaces. While the toolbox is designed primarily to process measurement data from physical transducers, it is also capable of simulating the fields radiated by transducer designs defined by the user. For instance, Section III-E uses a realistic holography-based boundary condition $V_0(x_r, y_q,\ z_{rq})$ at the surface of the transducer to simulate its entire 3-D field. However, an arbitrary distribution V_0 can be set as a boundary condition, allowing numerical experiments for various transducer designs with complex vibrational velocity patterns at the surface, such as multi-element arrays.

Key toolbox features include forward and backward field projections (for both CW and transient fields) and alignment of measured holograms with the physical transducer. In the case of a strongly focused transducer, the alignment is handled automatically based on the assumption that the center of curvature coincides with the pressure maximum of the focused field. The validity of this assumption mainly relies on the focusing angle (F-number) of the transducer for strongly focused transducers used in HIFU applications [16]. For instance, F-numbers of 0.75 and 1 considered in this study lead to shifts of 0.2 and 0.4 mm between the pressure maximum and the radius of curvature. This misalignment might result in minor degradation of the sharpness of the back-projected distribution and can be accounted for in the MATLAB/Octave code if desired. Notably, a different alignment approach that is not restricted to strongly focused transducers is also possible. From back-projections of transient holograms, the time-domain signal can be reconstructed over a volume that is expected to include the transducer surface. The actual surface can then be determined as the set of points where the non-zero vibration amplitudes begin at time zero. Such an approach will be studied in future work.

It is important to outline other limitations of the toolbox. The toolbox was designed for the far-field holography method, which does not capture near-field evanescent waves. Consequently, the reconstructed velocity pattern at transducer surfaces may exhibit small-scale heterogeneities in the velocity distribution. Nevertheless, far-field projections are accurate, as demonstrated in Section III-G.

The focus-sharpening feature, applied after hologram alignment, is based on visual inspection of the back-projected distribution and is not tied to any quantitative metrics. While this approach is generally sufficient for visualizing transducer surface defects, users may prefer to save back-projected distributions for various radii of curvature and employ alternative sharpness metrics to formalize their analysis.

The toolbox does not account for attenuation in water, which could introduce errors at high frequencies. For instance, given the attenuation coefficient of 0.025 Np/m/MHz^2 in water at 20°C, pressure losses over a 1-cm distance for a 1-MHz acoustic wave are negligible, at less than 0.03% [38]. However, the losses increase to 2.5% at 10 MHz and 9.5% at 20 MHz, which may be significant for certain applications. We plan to consider adding a feature to account for attenuation in future releases, based on user feedback and requests.

It is also important to note that for high frequencies, such as 10–20 MHz, another challenge arises with the scanning procedure. As mentioned earlier, a reasonable spatial grid step for transient holograms is approximately one-third of the wavelength of the central frequency. For a 1-MHz wave, with a sound speed of 1500 m/s, this step size is 0.5 mm, which is suitable for most positioning systems and hydrophones. However, for 10 MHz and 20 MHz, the required step sizes reduce to 0.05 mm and 0.025 mm, respectively. At these scales, it is crucial to ensure that the hydrophone's active area is sufficiently small to accommodate these grid cell sizes and that the positioning system is precise enough to maintain a stable grid step at this resolution.

Possible applications of the toolbox related to transducer diagnostics include selection of optimal operating frequencies. If transient holography measurements are acquired and aligned back-projection to the transducer surface is performed, then the pattern of transducer vibrations can be visualized over the range of frequencies present in the measured hologram. In the case considered here, the back-projected vibrational velocity distribution at the nominal frequency of $f_0 = 1.25$ MHz (Fig. 6(c)) was less uniform than a slightly lower frequency of 1.2 MHz (Fig. 6(b)). Therefore, an optimized transducer manufacturing procedure could involve performing holography-based analysis before designing the electrical impedance matching.

Another diagnostic application involves utilization of time-domain back-projection results to help identify various manufacturing defects. This approach can show small-scale defects like the wavefront asymmetry of the surface wave in the lens (Fig. 6(f)). Such defects do not affect the piston vibrations of the source surface (Fig. 6(d), (e)) or the symmetry of the focal lobe (Fig. 5(b)), but could influence the robustness and longevity of the transducer. For example, the lens of Transducer 1 with the observed surface-wave defect delaminated at the site of the defect after several histotripsy experiments.

Beyond the simulation regimes used in the demonstration examples presented here, others are available in the xDDx toolbox and may be helpful for certain applications. For instance, back-projection of a boundary condition from a spherical to a flat surface can be used to set a boundary condition for spherically shaped transducers on a plane. It can be one of possible simple methods for setting flat boundary conditions for spherically shaped transducers in other simulation software such as k-Wave (http://k-wave.org/), FOCUS (https://www.egr.msu.edu/~fultras-web/), and mSOUND (https://m-sound.github.io/mSOUND) [39– 41].

Examples of implementing this type of boundary condition are presented in our prior studies [42 – 45].

The xDDx toolbox presented here has multiple capabilities related to transducer characterization and diagnostics. The software was optimized to be compatible with different types of computer hardware; while the authors recommend using GPUs for simulations due to significant speed advantages (Table I), CPU-based configurations are also viable. Typical simulation times do not exceed 1 hour even for a 10-year-old Intel Core i7-6700K, Skylake CPU (see Section III-F).

Importantly, this paper does not cover all capabilities of the software. For example, the paper focuses on automatic and semi-manual alignment for focused transducers. However, the "Semi-Manual Alignment" tool (Section III-D) is also applicable to unfocused transducers, including plane-wave and divergence-wave sources. This tool allows users to manually identify symmetrical patterns in a forward-projected 3D field and determine the alignment parameters for subsequent hologram alignment.

Another "Pre-Defined Alignment" tool is useful for holograms of multi-element arrays that generate non-symmetrical field patterns. For these arrays, two holograms with the same transducer position in the tank can be measured: one with the element phases specifically set to form a tight focal lobe, and the other with a phase distribution of interest. Automatic alignment can then be performed for the first, focused case, and the alignment parameters can be saved using xDDx tools. These saved pre-defined alignment parameters can subsequently be applied to align the second hologram with an asymmetric beam.

Finally, the toolbox provides a "Validation Tool" that automatically creates a model of an idealized flat or spherical piston transducer with a specified grid discretization step, performs numerical xDDx field simulations for this transducer and compares the results to the analytical solution. This tool can be used to test different transducer models with varying sizes, frequencies, and grid discretization steps to evaluate simulation precision for specific cases of interest.

Users can refer to the user manual for more examples and technical details [30].

Acknowledgment

P.B. Rosnitskiy and T.D. Khokhlova are with the Department of Medicine, Division of Gastroenterology, University of Washington, Seattle, WA 98104 USA (e-mail: pavrosni@uw.edu).

O.A. Sapozhnikov and V.A. Khokhlova are with the Applied Physics Laboratory, University of Washington, Seattle, WA 98105 USA, and also with M. V. Lomonosov Moscow State University, 119991 Moscow, Russia

W. Kreider, G. Thomas, and K. Contreras are with the Applied Physics Laboratory, University of Washington, Seattle, WA 98105 USA

S.A. Tsysar is with the Faculty of Physics, M. V. Lomonosov Moscow State University, 119991 Moscow, Russia

References

[1] G. R. Harris, "Progress in medical ultrasound exposimetry," *IEEE Trans. Ultrason., Ferroelect., Freq. Control*, vol. 52, no. 5, pp. 717–736, May 2005.

[2] B. Zeqiri and M. Hodnett, "Measurements, phantoms, and standardization," *Proceedings of the Institution of Mechanical Engineers, Part H: Journal of Engineering in Medicine*, vol. 224, no. 2. SAGE Publications, pp. 375–391, Nov. 13, 2009.

[3] *Ultrasonics - Hydrophones - Part 1: Measurement and characterization of medical ultrasonic fields*, International Electrotechnical Commission standard IEC 62127-1, 2022.

[4] G. R. Harris *et al.*, "Hydrophone Measurements for Biomedical Ultrasound Applications: A Review," *IEEE Trans. Ultrason., Ferroelect., Freq. Control*, vol. 70, no. 2, pp. 85–100, Feb. 2023.

[5] J. D. Maynard, E. G. Williams, and Y. Lee, "Nearfield acoustic holography: I. Theory of generalized holography and the development of NAH," *The Journal of the Acoustical Society of America*, vol. 78, no. 4. Acoustical Society of America (ASA), pp. 1395–1413, Oct. 01, 1985.

[6] M. E. Schafer and P. A. Lewin, "Transducer characterization using the angular spectrum method," *The Journal of the Acoustical Society of America*, vol. 85, no. 5. Acoustical Society of America (ASA), pp. 2202–2214, May 01, 1989.

[7] O. A. Sapozhnikov, Yu. A. Pishchal'nikov, and A. V. Morozov, "Reconstruction of the normal velocity distribution on the surface of an ultrasonic transducer from the acoustic pressure measured on a reference surface," *Acoustical Physics*, vol. 49, no. 3. Pleiades Publishing Ltd, pp. 354–360, May 2003.

[8] O. A. Sapozhnikov, S. A. Tsysar, V. A. Khokhlova, and W. Kreider, "Acoustic holography as a metrological tool for characterizing medical ultrasound sources and fields," *The Journal of the Acoustical Society of America*, vol. 138, no. 3. Acoustical Society of America (ASA), pp. 1515–1532, Sep. 01, 2015.

[9] *Ultrasonics–Field Characterization–Specification and Measurement of Field Parameters for High Intensity Therapeutic Ultrasound (HITU) Transducers and Systems*, International Electrotechnical Commission standard IEC TS 62556, 2014.

[10] G. ter Haar and C. Coussios, "High intensity focused ultrasound: Physical principles and devices," *International Journal of Hyperthermia*, vol. 23, no. 2. Informa UK Limited, pp. 89–104, Jan. 01, 2007.

[11] W. Kreider et al., "Characterization of a multi-element clinical HIFU system using acoustic holography and nonlinear modeling," *IEEE Trans. Ultrason., Ferroelect., Freq. Control*, vol. 60, no. 8, pp. 1683–1698, Aug. 2013.

[12] E. Martin, Y. T. Ling, and B. E. Treeby, "Simulating Focused Ultrasound Transducers Using Discrete Sources on Regular Cartesian Grids," *IEEE Trans. Ultrason., Ferroelect., Freq. Control*, vol. 63, no. 10, pp. 1535–1542, Oct. 2016.

[13] B. Treeby, F. Lucka, E. Martin, and B. T. Cox, "Equivalent-Source Acoustic Holography for Projecting Measured Ultrasound Fields Through Complex Media," *IEEE Trans. Ultrason., Ferroelect., Freq. Control*, vol. 65, no. 10, pp. 1857–1864, Oct. 2018.

[14] S. A. Ilyin, P. V. Yuldashev, V. A. Khokhlova, L. R. Gavrilov, P. B. Rosnitskiy, and O. A. Sapozhnikov, "Analytical method for evaluating the quality of acoustic fields radiated by a multielement therapeutic array with electronic focus steering," *Acoust. Phys.*, vol. 61, no. 1, pp. 52–59, Jan. 2015.

[15] M. A. Ghanem et al., "Field characterization and compensation of vibrational nonuniformity for a 256-element focused ultrasound phased array," *IEEE Trans. Ultrason., Ferroelectr., Freq. Control*, vol. 65, no. 9, pp. 1618–1630, Sep. 2018.

[16] P. B. Rosnitskiy et al., "Design of HIFU transducers for generating specified nonlinear ultrasound fields," *IEEE Trans. Ultrason., Ferroelectr., Freq. Control*, vol. 64, no. 2, pp. 374–390, Feb. 2017.

[17] P. B. Rosnitskiy, B. A. Vysokanov, L. R. Gavrilov, O. A. Sapozhnikov, and V. A. Khokhlova, "Method for designing multielement fully populated random phased arrays for ultrasound surgery applications," *IEEE Trans. Ultrason., Ferroelectr., Freq. Control*, vol. 65, no. 4, pp. 630–637, Apr. 2018.

[18] R. P. Williams et al., "Dual-Mode 1-D Linear Ultrasound Array for Image-Guided Drug Delivery Enhancement Without Ultrasound Contrast Agents," *IEEE Trans. Ultrason., Ferroelect., Freq. Control*, vol. 70, no. 7, pp. 693-707, 2023.

[19] E. Martin, M. Roberts, and B. Treeby, "Measurement and simulation of steered acoustic fields generated by a multielement array for therapeutic ultrasound," *JASA Express Letters*, vol. 1, no. 1, p. 012001, 2021.
[20] S. A. Tsysar, P. B. Rosnitskiy, S. A. Asfandiyarov, S. A. Petrosyan, V. A. Khokhlova, and O. A. Sapozhnikov, "Phase Correction of the Channels of a Fully Populated Randomized Multielement Therapeutic Array Using the Acoustic Holography Method," *Acoustical Physics*, vol. 70, no. 1. Pleiades Publishing Ltd, pp. 82–89, Feb. 2024.
[21] O. A. Sapozhnikov, A. E. Ponomarev, and M. A. Smagin, "Transient acoustic holography for reconstructing the particle velocity of the surface of an acoustic transducer," *Acoust. Phys.*, vol. 52, no. 3, pp. 324–330, 2006.
[22] S. A. Tsysar, D. A. Nikolaev, and O. A. Sapozhnikov, "Broadband Vibrometry of a Two-Dimensional Ultrasound Array Using Transient Acoustic Holography," *Acoustical Physics*, vol. 67, no. 3. Pleiades Publishing Ltd, pp. 320–328, May 2021.
[23] A. D. Maxwell, K. J. Haworth, C. K. Holland, S. A. Hendley, W. Kreider, and K. B. Bader, "Design and Characterization of an Ultrasound Transducer for Combined Histotripsy-Thrombolytic Therapy," *IEEE Trans. Ultrason., Ferroelect., Freq. Control*, vol. 69, no. 1, pp. 156–165, Jan. 2022.
[24] A. D. Maxwell *et al.*, "A Prototype Therapy System for Transcutaneous Application of Boiling Histotripsy," *IEEE Trans. Ultrason., Ferroelect., Freq. Control*, vol. 64, no. 10, pp. 1542–1557, Oct. 2017.
[25] M. A. Ghanem, A. D. Maxwell, D. Dalecki, O. A. Sapozhnikov, and M. R. Bailey, "Phase holograms for the three-dimensional patterning of unconstrained microparticles," *Scientific Reports*, vol. 13, no. 1. Springer Science and Business Media LLC, Jun. 06, 2023.
[26] D. A. Nikolaev, S. A. Tsysar, V. A. Khokhlova, W. Kreider, and O. A. Sapozhnikov, "Holographic extraction of plane waves from an ultrasound beam for acoustic characterization of an absorbing layer of finite dimensions," *The Journal of the Acoustical Society of America*, vol. 149, no. 1. Acoustical Society of America (ASA), pp. 386–404, Jan. 01, 2021.
[27] D. A. Nikolaev, S. A. Tsysar, and O. A. Sapozhnikov, "Determination and Compensation of Axes Misalignment of Three-Coordinate Positioning Systems Using Acoustic Holography," Bulletin of the Russian Academy of Sciences: Physics, vol. 85, no. 6. Allerton Press, pp. 658–664, Jun. 2021.
[28] A. Z. Kaloev, D. A. Nikolaev, V. A. Khokhlova, S. A. Tsysar, and O. A. Sapozhnikov, "Spatial Correction of an Acoustic Hologram for Reconstructing Surface Vibrations of an Axially Symmetric Ultrasound Transducer," *Acoustical Physics*, vol. 68, no. 1. Pleiades Publishing Ltd, pp. 71–82, Feb. 2022.
[29] M. Frigo and S. G. Johnson, "FFTW: an adaptive software architecture for the FFT," Proceedings of the 1998 IEEE International Conference on Acoustics, *Speech and Signal Processing*, ICASSP '98 (Cat. No.98CH36181), vol. 3. IEEE, pp. 1381–1384.
[30] P. B. Rosnitskiy, O. A. Sapozhnikov, V. A. Khokhlova, W. Kreider, T. D. Khokhlova *xDDx: User Manual* [Online]. Available: https://github.com/pavrosni/xDDx/releases
[31] G. Guennebaud (May, 15, 2013) *Eigen: a C++ linear algebra library* [Online]. Available: https://eigen.tuxfamily.org/
[32] O. A. Sapozhnikov and M. R. Bailey, "Radiation force of an arbitrary acoustic beam on an elastic sphere in a fluid," *The Journal of the Acoustical Society of America*, vol. 133, no. 2. Acoustical Society of America (ASA), pp. 661–676, Jan. 30, 2013.
[33] H. T. O'Neil, "Theory of Focusing Radiators," *The Journal of the Acoustical Society of America*, vol. 21, no. 5. Acoustical Society of America (ASA), pp. 516–526, Sep. 01, 1949.
[34] D. A. Freedman, *Statistical Models Theory and Practice*, New York, NY, USA: Cambridge University Pres, 2009.
[35]T. Khokhlova *et al.*, "Dependence of inertial cavitation induced by high intensity focused ultrasound on transducer F-number and nonlinear waveform distortion," *The Journal of the Acoustical Society of America*, vol. 144, no. 3. Acoustical Society of America (ASA), pp. 1160–1169, Sep. 01, 2018.
[36] D. Cathignol, O. A. Sapozhnikov, and J. Zhang, "Lamb waves in piezoelectric focused radiator as a reason for discrepancy between O'Neil's formula and experiment," *The Journal of the Acoustical Society of America*, vol. 101, no. 3. Acoustical Society of America (ASA), pp. 1286–1297, Mar. 01, 1997.
[37] O. A. Sapozhnikov and M. A. Smagin, "Finding the dispersion relations for lamb-type waves in a concave piezoelectric plate by optical visualization of the ultrasound field radiated into a fluid," *Acoustical Physics*, vol. 61, no. 2. Pleiades Publishing Ltd, pp. 181–187, Mar. 2015.
[38]F. A. Duck, *Physical Properties of Tissues: A Comprehensive Reference Book*. New York, NY, USA: Academic Press, 2013.
[39] B. E. Treeby and B. T. Cox, "k-Wave: MATLAB toolbox for the simulation and reconstruction of photoacoustic wave fields," *J. Biomed. Opt.*, vol. 15, no. 2, 2010, Art. no. 021314.
[40] D. Chen and R. J. McGough, "A 2D fast near-field method for calculating near-field pressures generated by apodized rectangular pistons," *The Journal of the Acoustical Society of America*, vol. 124, no. 3. Acoustical Society of America (ASA), pp. 1526–1537, 2008.
[41] J. Gu and Y. Jing, "mSOUND: An Open Source Toolbox for Modeling Acoustic Wave Propagation in Heterogeneous Media," *IEEE Transactions on Ultrasonics, Ferroelectrics, and Frequency Control*, vol. 68, no. 5, pp. 1476–1486, 2021.
[42] P. B. Rosnitskiy, P. V. Yuldashev, O. A. Sapozhnikov, L. R. Gavrilov, and V. A. Khokhlova, "Simulation of nonlinear trans-skull focusing and formation of shocks in brain using a fully populated ultrasound array with aberration correction," *The Journal of the Acoustical Society of America*, vol. 146, no. 3. Acoustical Society of America (ASA), pp. 1786–1798, Sep. 01, 2019.
[43] D. D. Chupova, P. B. Rosnitskiy, L. R. Gavrilov, and V. A. Khokhlova, "Compensation for Aberrations of Focused Ultrasound Beams in Transcranial Sonications of Brain at Different Depths," *Acoustical Physics*, vol. 68, no. 1. Pleiades Publishing Ltd, pp. 1–10, Feb. 2022.
[44] P. B. Rosnitskiy, T. D. Khokhlova, G. R. Schade, O. A. Sapozhnikov, and V. A. Khokhlova, "Treatment Planning and Aberration Correction Algorithm for HIFU Ablation of Renal Tumors," *IEEE Trans. Ultrason., Ferroelect., Freq. Control*, vol. 71, no. 3, pp. 341–353, Mar. 2024.
[45] M. M. Karzova *et al.*, "Comparative Characterization of Nonlinear Ultrasound Fields Generated by Sonalleve V1 and V2 MR-HIFU Systems," *IEEE Trans. Ultrason., Ferroelect., Freq. Control*, vol. 70, no. 6, pp. 521–537, Jun. 2023.

Pavel B. Rosnitskiy received the M.S. degree in physics and Ph.D. degree in acoustics from Moscow State University (MSU), Moscow, Russia, in 2016 and 2019, respectively. Following graduation from the Ph.D. program he was appointed as a Junior Research Scientist with the Department of Medical Physics, Physics Faculty, MSU. He is currently pursuing postdoctoral training at the Department of Medicine, University of Washington (UW), Seattle. His research interests include nonlinear acoustics, ultrasound imaging, design of multielement arrays, and therapeutic applications of high-intensity focused ultrasound waves with shocks.

Oleg A. Sapozhnikov received his M.S. degree in physics in 1985 and Ph.D. and D.Sc. degrees in acoustics in 1988 and 2008, respectively, from Moscow State University (MSU), Moscow, Russia. He is currently a Professor in the Department of Acoustics of the Physics Faculty of MSU. Since 1996, he is also affiliated with the Center for Industrial and Medical Ultrasound in the Applied Physics Laboratory at the University of Washington. His research interests are physical acoustics, nonlinear wave phenomena, medical ultrasound including shock wave lithotripsy, high intensity focused ultrasound, and ultrasound-based imaging.

Vera A. Khokhlova received the M.S. degree in physics and the Ph.D. and D.Sc. degrees in acoustics from Lomonosov Moscow State University (MSU), Moscow, Russia, in 1986, 1991, and 2012, respectively.
After her graduation from the Ph.D. program, she was appointed by Lomonosov Moscow State University, where she is currently an Associate Professor with the Department of Acoustics, Physics Faculty. Since 1995, she has been with the Center for Industrial and Medical Ultrasound, Applied Physics Laboratory (APL), University of Washington, Seattle, WA, USA. Her research interests are in the field of nonlinear acoustics, therapeutic ultrasound including metrology and bioeffects of high intensity focused ultrasound fields, shock wave focusing, nonlinear wave propagation in inhomogeneous media, and nonlinear modeling.

Wayne Kreider received the B.S. and M.S. degrees in engineering mechanics at Virginia Tech, Blacksburg, VA, USA, in 1993 and 1995, respectively, and the Ph.D. degree in bioengineering from the University of Washington, Seattle, WA, USA, in 2008. He is a licensed Professional Engineer in the Commonwealth of Virginia. He was an Engineer with Naval Surface Warfare Center, Dahlgren, VA, USA, and Dominion Engineering Inc., Reston, VA, USA. Since 2001, he has been with the Applied Physics Laboratory (APL), Center for Industrial and Medical Ultrasound, University of Washington. His research interests include acoustic cavitation, transport processes in oscillating bubbles, therapeutic ultrasound, and ultrasound metrology.

Sergey A. Tsysar received the M.S. degree in physics in 2008 and the Ph.D. degree in acoustics in 2011 from Moscow State University (MSU), Moscow, Russia. After graduation from the Ph.D. program, he was appointed by MSU, where he is currently an Associate Professor with the Faculty of Physics. His research interests are inverse problems in acoustics, acoustic holography, transducers characterization, and medical applications, high-intensity focused ultrasound (HIFU), acoustic radiation force application for particle manipulation and scaffold-free biofabrication.

Gilles P.L. Thomas received the Engineering degree in general engineering from the École Centrale de Nantes, Nantes, France, in 2014, the Engineering degree in mechatronics engineering and the M.S. degree in control and automation engineering from the Polytechnic School, University of São Paulo, São Paulo, Brazil, in 2014 and 2015, respectively, and the Ph.D. degree in biomedical engineering from the Université Lyon 1, Lyon, France, in 2019. His research interests include HIFU aberration correction, cavitation-based therapeutic ultrasound, and nonlinear acoustics.

Kaizer Contreras received the B.S. degree in mechanical engineering from the University of Washington, Seattle, WA, USA, in 2020. He is currently a Researcher at the Center of Industrial Medical Ultrasound, Applied Physics Laboratory, University of Washington. His current research interests include neuromodulation, cryopreservation, histotripsy, and lithotripsy. Mr. Contreras received the 3-D Design Certificate of Accomplishment from Bellevue College in 2021. He holds the Vice Chair seat at the IEEE–UFFC-Seattle Chapter.

Tatiana D. Khokhlova received her Ph.D. degree in physics from Moscow State University (MSU), Moscow, Russia, in 2008.

After graduation from the Ph.D. program, she moved to the University of Washington (UW), Seattle, WA, USA, for postdoctoral training at the Applied Physics Laboratory. She is currently an Associate Professor of Research with the Department of Medicine, UW. Her research interests are in physical acoustics, cavitation-based therapeutic ultrasound applications and ultrasound imaging methods for therapy guidance.